

THE EVOLUTION OF GALAXY NUMBER DENSITY AT  $z < 8$  AND ITS IMPLICATIONSCHRISTOPHER J. CONSELICE, AARON WILKINSON, KENNETH DUNCAN<sup>1</sup>, AND ALICE MORTLOCK<sup>2</sup>

University of Nottingham, School of Physics &amp; Astronomy, Nottingham, NG7 2RD, UK

Received 2016 February 29; revised 2016 June 21; accepted 2016 July 6; published 2016 October 14

## ABSTRACT

The evolution of the number density of galaxies in the universe, and thus also the total number of galaxies, is a fundamental question with implications for a host of astrophysical problems including galaxy evolution and cosmology. However, there has never been a detailed study of this important measurement, nor a clear path to answer it. To address this we use observed galaxy stellar mass functions up to  $z \sim 8$  to determine how the number densities of galaxies change as a function of time and mass limit. We show that the increase in the total number density of galaxies ( $\phi_T$ ), more massive than  $M_* = 10^6 M_\odot$ , decreases as  $\phi_T \sim t^{-1}$ , where  $t$  is the age of the universe. We further show that this evolution turns over and rather increases with time at higher mass lower limits of  $M_* > 10^7 M_\odot$ . By using the  $M_* = 10^6 M_\odot$  lower limit we further show that the total number of galaxies in the universe up to  $z = 8$  is  $2.0^{+0.7}_{-0.6} \times 10^{12}$  (2 trillion), almost a factor of 10 higher than would be seen in an all sky survey at Hubble Ultra-Deep Field depth. We discuss the implications for these results for galaxy evolution, as well as compare our results with the latest models of galaxy formation. These results also reveal that the cosmic background light in the optical and near-infrared likely arise from these unobserved faint galaxies. We also show how these results solve the question of why the sky at night is dark, otherwise known as Olbers' paradox.

**Key words:** galaxies: evolution – galaxies: fundamental parameters – galaxies: general – galaxies: high-redshift – galaxies: luminosity function, mass function – galaxies: structure

## 1. INTRODUCTION

When discovering the universe and its properties we are always interested in knowing absolutes. For example, it is of astronomical interest to calculate how many stars are in our Galaxy, how many planets are surrounding these stars (Fressin et al. 2013), and the total mass density of the universe (e.g., Fukugita & Peebles 2004), among other absolutes in the universe's properties. One of these that has only been answered in a rough way is the total number density of galaxies, and thus also the total number of galaxies in the universe.

This question is not only of passing interest as a curiosity, but is also connected to many other questions in cosmology and astronomy. The evolution of the number densities of galaxies relates to issues such as galaxy formation/evolution through the number of systems formed, the evolution of the ratio of giant galaxies to dwarf galaxies, the distant supernova and gamma-ray burst rate, the star formation rate of the universe, and how new galaxies are created/destroyed through mergers (e.g., Bridge et al. 2007; Lin et al. 2008; Jogle et al. 2009; Conselice et al. 2011; Bluck et al. 2012; Conselice 2014; Ownsworth et al. 2014). The number of galaxies in the observable universe also divulges information about the mass density of the universe and background light at various wavelengths, as well as insights into Olbers' Paradox. However, there still does not yet exist a good measurement for this fundamental quantity.

Understanding the co-moving number density evolution of galaxies has only been possible in any meaningful way since deep imaging with telescopes began with the advent of CCD cameras. Deep surveys to search for distant galaxies started in the 1990s (e.g., Koo & Kron 1992; Steidel & Hamilton 1992;

Djorgovski et al. 1995), and reached our current depths after deep *Hubble Space Telescope* (HST) imaging campaigns were carried out, especially within the Hubble Deep Field (Williams et al. 1996). This was later expanded to other deep fields such as the Hubble Deep Field South (Williams et al. 2000), the Great Observatories Origins Survey (Giavalisco et al. 2004), and the near-infrared CANDELS fields (Grogin et al. 2011; Koekemoer et al. 2011), and finally to the Hubble Ultra-Deep Field (HUDF; Beckwith et al. 2006), which remains the deepest image in the optical and near-infrared of our universe taken to date.

However, despite these surveys it is still uncertain how the total number density of galaxies evolves over time. This is an interesting question as we know that the star formation rate rises, and then declines at  $z < 8$  (e.g., Bouwens et al. 2009; Duncan et al. 2014; Madau & Dickinson 2014), while at the same time galaxies become larger and less peculiar (e.g., Conselice et al. 2004; Papovich et al. 2005; Buitrago et al. 2013; Mortlock et al. 2013; Lee et al. 2013; Conselice 2014; Boada et al. 2016). However, we do not know how the total number of galaxies at a given epoch evolves, and how this is associated with the general formation of the galaxy population as a whole.

There are a few reasons for why deep imaging programs are not easily able to convert observations to total numbers of galaxies. One of these issues is that all deep observations are incomplete. This is due to limitations in exposure times and depth such that certain galaxies will be detected more readily than other galaxies. The result of this is an incompleteness down to the magnitude limit of even the deepest surveys, which can be corrected for, but which still leaves some uncertainty. However, the more important issue is that these observations do not reach the faintest galaxies, although from number density fits and theory we know that there should be many more faint galaxies beyond our current observational limits.

<sup>1</sup> Present address: Leiden Observatory, Leiden University, P.O. Box 9513, 2300 RA Leiden, The Netherlands.

<sup>2</sup> Present address: SUPA, Institute for Astronomy, University of Edinburgh, Royal Observatory, Edinburgh, EH9 3HJ, UK.

It is also important to address what we mean by the total number density of galaxies in the universe. This is not a simple quantity to define as the total number density that exists now, the total number density that is observable in principle, and the total number density that is observable with current technology, are all different questions with different answers. There is also the issue that we are limited by the cosmological horizon over what we can observe, and therefore there are galaxies we cannot see beyond it. Even the number of galaxies that exist in the universe today, i.e., if we could view the entire universe as it is, and not be limited by light travel time, is a complicated question. Galaxies in the distant universe have evolved beyond what we can currently observe due to the finite nature of the speed of light, and presumably would look similar to those in the local universe. We address these issues in the paper. Our default and ultimate total number density of galaxies we investigate in this paper is how the number density evolves within the current observable universe up to  $z \sim 8$ .

For comparison purposes, we also carry out an analysis in the [Appendix](#) of the number of galaxies that are visible to modern telescopes, at all wavelengths, which we can currently observe. We then compare this to measurements of the total number that actually can be potentially observed in the universe based on measured mass functions. We also discuss how these results reveal information concerning galaxy evolution and background light. We also give indications for future surveys and what fraction of galaxies these will observe.

This paper is divided up into several sections. Section 2 describes the data we use throughout this analysis, Section 3 describes the results of this paper including using fits of galaxy stellar mass functions to derive the total number of galaxies that are in the universe. Section 4 describes the implications of these results and Section 5 is a summary. Throughout this paper we use a standard cosmology of  $H_0 = 70 \text{ km s}^{-1} \text{ Mpc}^{-1}$ , and  $\Omega_m = 1 - \Omega_\Lambda = 0.3$ .

## 2. DATA

The data we use for this paper come from many sources, and results from previous papers. In the [Appendix](#) we describe how many galaxies we can actually observe at present in the universe, based on the deepest observations yet available. Here in the main paper we address the question of how many galaxies are potentially detectable within the universe if deep imaging, over all wavelengths, could be carried out in every location of the sky without any interference from the Galaxy, or other contamination.

For the bulk analysis and results of this paper we utilize mass functions of galaxies from the local universe up until  $z \sim 8$  to determine how the number density of galaxies evolves with time and redshift. These mass and luminosity functions are now just starting to be measured at high redshifts, and our primary data originates from mass functions calculated using deep and wide near-infrared and optical surveys with *HST* and ground-based telescopes.

As described in the next section, the mass functions we utilize are from Perez-Gonzalez et al. (2008), Kajisawa et al. (2009), Fontana et al. (2004, 2006), Caputi et al. (2011), Pozzetti et al. (2007), Mortlock et al. (2011), Muzzin et al. (2013), Tomczak et al. (2014), and Mortlock et al. (2015) for galaxies at  $z < 3$ . At the highest redshifts we use mass functions published in Duncan et al. (2014), Grazian et al. (2015), Caputi et al. (2011), and Song et al. (2016). We

normalize all of these mass functions for each survey based on the Salpeter initial mass function (IMF) for stars between  $0.1 M_\odot$  and  $100 M_\odot$ . We also use only the co-moving number densities from these mass functions, using co-moving volumes, as opposed to physical volumes. This tells us how the number of galaxies is evolving in the same effective volume, with the effects of the Hubble expansion removed. These mass functions are shown in Figure 1 down to the mass limit in which they are complete based on all of these various surveys, which are also listed in Table 1.

## 3. THE EVOLUTION OF GALAXY NUMBER DENSITY

### 3.1. Introduction and Caveats

The primary method we use to determine the number densities of galaxies in the universe is to integrate through the fitted mass functions the number of galaxies that are at a given redshift. This requires extrapolating fitted stellar mass functions to reach down to a low mass limit of the galaxy population. There are many ways in which this can be done, which we discuss below. One of the most important questions is the lower limit at which we should count galaxies from the mass functions. Due to the recent publication of stellar mass functions up to  $z \sim 8$  (e.g., Duncan et al. 2014; Grazian et al. 2015; Song et al. 2016) we can now make this calculation for the first time. Another issue is whether or not the Schechter function can be extrapolated below the limit of the data in which it was originally fit. This is a question we investigate in detail.

This is complementary to the directly observed approach presented in the [Appendix](#), and is a more accurate way to measure the number of galaxies in the currently observable universe, if the mass functions are properly measured and parameterized accurately. However, this method is potentially fraught with pitfalls that have to be carefully considered and addressed, not the least of which is that this measurement relies on much more than simple photometry and detection issues, which are also present when simply measuring the number of galaxies. The situation here involves other uncertainties involving the measurements of stellar masses and redshifts. Nonetheless, if we can account for these uncertainties, the integration of fitted mass functions can tell us the number densities of galaxies within a given redshift interval with some measured uncertainty.

We use this method to calculate the total number density of galaxies that are within the currently observable universe as a function of redshift. To do this we do not directly integrate the observed mass functions, but use a parameterized fitted form as given by the Schechter (1976) function to determine the total number densities of galaxies as a function of redshift. The form of this function is given by

$$\phi(M) = b \times \phi^* \ln(10) [10^{b(M-M^*)}]^{(1+\alpha)} \exp[-10^{b(M-M^*)}] \quad (1)$$

where  $b = 1$  for the mass function and  $b = 0.4$  for the luminosity function, which would be written in terms of absolute magnitudes. For the mass function,  $M^*$  is the characteristic mass in log units and determines where the mass function changes slope, and  $M = \log(M_*/M_\odot)$ , is the mass in log units. Similarly for the luminosity function,  $M^*$  corresponds to the characteristic magnitude. For both functions  $\phi^*$  is the

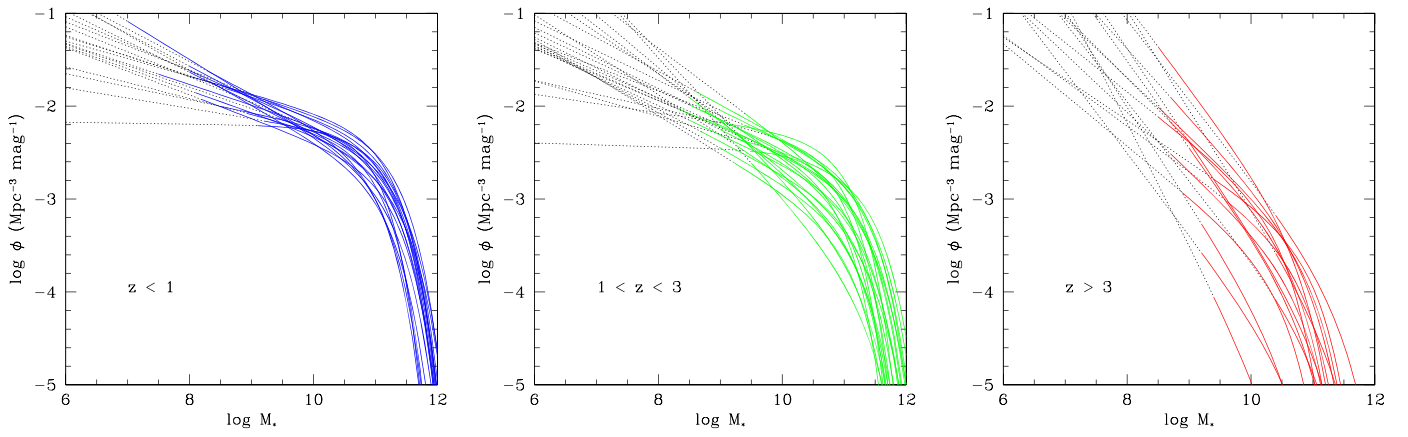


**Figure 1.** Mass functions that we use throughout this paper, plotted through best-fitting Schechter function fits. These are all from the various studies described in Section 2. The mass functions are shown in terms of redshifts, such that the left panel shows systems at  $z < 1$ , the middle panel shows  $1 < z < 3$ , the far right panel shows  $z > 3$ . These mass functions are shown such that the solid colored lines are the mass functions down to the limit of the respective data whereby it is complete, and the dotted lines show our extrapolation down to  $M_* = 10^6 M_\odot$ . The “flattest” mass function plot in the  $1 < z < 3$  regime is from Muzzin et al. (2013) and the flattest  $z > 3$  mass function is from Grazian et al. (2015).

normalization, and  $\alpha$  determines the slope for fainter and lower mass galaxies. Our method is to use published values of  $\phi^*$ ,  $\alpha$ , and  $M^*$  to calculate the integrated number of galaxies within different redshift bins.

We use the Schechter function as a tool to calculate the total number density as overall it does a good job of representing the distribution of galaxy masses at all redshifts in the ranges where we probe. We do not, however, know at what lower mass limit it remains valid, which is one uncertainty in our analysis. We discuss the use of a  $M_* > 10^6 M_\odot$  limit below and the justification for using this as our lower limit. We also discuss how our results would change if we were to use a different lower mass cut-off limit.

Because we are integrating these mass functions throughout the universe’s history we must use a variety of surveys to account for the number of galaxies at different redshifts. Different redshift ranges require surveys done at different wavelengths, and various surveys have found sometimes differing values for the Schechter parameters. In this paper we attempt a comprehensive examination of these mass functions, which, particularly at low redshift, can give widely divergent number densities and forms of evolution. We find nearly identical results if we use the double forms of Schechter fits sometimes presented for the fits to mass functions at lower redshifts, or if we use power-law fits to the mass functions for the highest redshift galaxies.

Between redshifts  $z \sim 0$ –3 we use the fitted mass function parameter values and their errors from surveys carried out by Perez-Gonzalez et al. (2008), Kajisawa et al. (2009), Fontana et al. (2004, 2006), Caputi et al. (2011), Pozzetti et al. (2007), Marchesini et al. (2009), and Mortlock et al. (2011, 2015). These are stellar mass functions are determined by measuring the stellar masses of objects via spectral energy distribution (SED) fitting. While there is a large scatter in the various measurements of the Schechter function parameters, we use all this information to take into account different measurement and fitting methods as well as cosmic variance from the different fields used. These mass functions, as parameterized by the Schechter function, are shown in Figure 1. We also convert those studies that use a Chabrier IMF—which are Pozzetti et al. (2007), Duncan et al. (2014), Mortlock et al. (2015), and Muzzin et al. (2013) who uses a Kroupa IMF into a Salpeter

IMF. The list of values we use in our analysis is shown in Table 1.

Note that we only consider those mass functions where the parameter  $\alpha$  in the Schechter fit was allowed to vary. If a mass function result is obtained from fixing the value of  $\alpha$ , this biases the number of galaxies, as this value has a major impact on the number of fainter, and lower mass, galaxies in given volume (Section 3.2). We therefore exclude mass function results from studies that hold  $\alpha$  constant when fitting for the other Schechter parameters.

Recently, the first measurements of the stellar mass function at high redshifts up to  $z \sim 8$  allows for this procedure to be carried out back to when we can study the earliest galaxies discovered to date. The mass functions we use come from Duncan et al. (2014) who use data from the GOODS-S CANDELS field, Grazian et al. (2015) who use GOODS-S and GOODS-N CANDELS data, and GOODS-S/N CANDELS and HUDF data from Song et al. (2016).

At higher redshifts mass functions are relatively new, and thus we also examine observed luminosity functions in the ultraviolet, typically at 1500 Å, to test for consistency. For this we use the luminosity functions published in Bouwens et al. (2011, 2015), McLure et al. (2009, 2013), and Finkelstein et al. (2015). McLure et al. (2013) and Bouwens et al. (2015) discuss the results from the deepest *HST* data including the HUDF12 survey, which probes galaxies to the highest redshifts at  $z = 8$  and  $z = 9$ .

To convert our stellar mass limit to a UV magnitude limit we use the relations between these two quantities as calculated in Duncan et al. (2014). Duncan et al. (2014) fit the linear relation between the mass and light in the UV and how it evolves with redshift. We use these to determine the UV limit corresponding to our default mass limit of  $M_* = 10^6 M_\odot$ . This thereby permits us to associate our stellar mass limit with a limit in absolute magnitude in the UV. We do not use these values in our calculations, but use these luminosity functions to check consistency with our results from the stellar mass functions. We find a high consistency with the stellar mass functions, including when we use the different variations on the conversion between stellar mass and UV luminosity (e.g., Duncan et al. 2014; Song et al. 2016). Furthermore, our high- $z$  mass functions all more or less agree at high redshift, with the

**Table 1**  
Schechter Function Parameters

Redshift ( $z$ )	$\alpha$	$\log M^*$ ( $M_\odot$ )	$\phi^*$ ( $\times 10^{-4}$ ) ( $\text{Mpc}^{-3}$ )	Limit $\log M_*$	References
(1)	(2)	(3)	(4)	(5)	(6)
0.20–0.40	$-1.19 \pm 0.08$	$11.20 \pm 0.10$	$22.4 \pm 6.0$	8.0	Perez-Gonzalez+08
0.20–0.50	$-1.29 \pm 0.01$	$11.44 \pm 0.03$	$12.2 \pm 0.5$	8.0	Muzzin+13
0.20–0.50	$-1.35 \pm 0.04$	$11.27 \pm 0.10$	$10.9 \pm 2.8$	8.0	Tomczak+14
0.20–0.70	$-1.11 \pm 0.10$	$11.22^{+0.13}_{-0.12}$	18.2	9.2	Fontana+04
0.30–0.50	$-1.41 \pm 0.02$	$11.54 \pm 0.07$	$6.3 \pm 1.3$	7.0	Mortlock+13
0.40–0.60	$-1.22 \pm 0.07$	$11.26 \pm 0.11$	$17.4 \pm 4.5$	8.6	Perez-Gonzalez+08
0.40–0.60	$-1.22 \pm 0.02$	$11.23 \pm 0.03$	$14.3 \pm 1.0$	7.5	Fontana+06 <sup>a</sup>
0.40–0.70	$-1.14^{+0.04}_{-0.04}$	$11.15 \pm 0.06$	$18.3 \pm 2.4$	8.5	Pozzetti+07
0.50–0.75	$-1.35 \pm 0.04$	$11.22 \pm 0.06$	$11.7 \pm 2.1$	8.3	Tomczak+14
0.50–1.00	$-1.17 \pm 0.01$	$11.22 \pm 0.02$	$16.3 \pm 0.6$	8.9	Muzzin+13
0.50–1.00	$-1.34 \pm 0.02$	$11.38 \pm 0.04$	$7.6 \pm 0.9$	8.0	Mortlock+13
0.50–1.00	$-1.21^{+0.03}_{-0.02}$	$11.31^{+0.07}_{-0.08}$	$18.6 \pm 2.4$	8.5	Kajisawa+09
0.60–0.80	$-1.26 \pm 0.08$	$11.25 \pm 0.08$	$15.1 \pm 3.7$	9.2	Perez-Gonzalez+08
0.60–0.80	$-1.24 \pm 0.03$	$11.24 \pm 0.04$	$10.9 \pm 1.0$	8.1	Fontana+06 <sup>a</sup>
0.70–0.90	$-1.01^{+0.07}_{-0.08}$	$10.89 \pm 0.06$	$26.0 \pm 3.8$	9.1	Pozzetti+07
0.70–1.00	$-1.27 \pm 0.10$	$11.37^{+0.22}_{-0.21}$	11.0	10.4	Fontana+04
0.75–1.00	$-1.38 \pm 0.04$	$11.38 \pm 0.12$	$6.8 \pm 1.9$	8.4	Tomczak+14
0.80–1.00	$-1.23 \pm 0.09$	$11.27 \pm 0.09$	$12.3 \pm 3.4$	9.4	Perez-Gonzalez+08
0.80–1.00	$-1.25 \pm 0.03$	$11.26 \pm 0.05$	$8.5 \pm 0.9$	8.2	Fontana+06 <sup>a</sup>
0.90–1.20	$-1.10^{+0.07}_{-0.08}$	$11.00 \pm 0.06$	$18.3 \pm 2.8$	9.2	Pozzetti+07
1.00–1.25	$-1.33 \pm 0.05$	$11.31 \pm 0.10$	$6.5 \pm 1.9$	8.7	Tomczak+14
1.00–1.30	$-1.26 \pm 0.04$	$11.31 \pm 0.11$	$8.7 \pm 2.0$	9.4	Perez-Gonzalez+08
1.00–1.40	$-1.28 \pm 0.04$	$11.26 \pm 0.07$	$6.2 \pm 0.8$	8.3	Fontana+06 <sup>a</sup>
1.00–1.50	$-1.36 \pm 0.05$	11.43	$6.0 \pm 1.1$	8.6	Mortlock+11
1.00–1.50	$-1.32^{+0.04}_{-0.04}$	$11.36^{+0.13}_{-0.10}$	$6.9 \pm 1.4$	9.0	Kajisawa+09
1.00–1.50	$-1.31 \pm 0.03$	$11.26 \pm 0.04$	$6.2 \pm 0.9$	8.5	Mortlock+13
1.20–1.60	$-1.15^{+0.12}_{-0.12}$	$10.94 \pm 0.07$	$14.8 \pm 3.0$	9.8	Pozzetti+07
1.25–1.50	$-1.29 \pm 0.05$	$11.10 \pm 0.05$	$7.8 \pm 1.6$	8.8	Tomczak+14
1.30–1.60	$-1.29 \pm 0.08$	$11.34 \pm 0.10$	$5.4 \pm 2.0$	9.8	Perez-Gonzalez+08
1.40–1.80	$-1.31 \pm 0.06$	$11.25 \pm 0.11$	$4.3 \pm 0.7$	8.5	Fontana+06 <sup>a</sup>
1.50–2.00	$-1.51 \pm 0.03$	$11.37 \pm 0.06$	$1.8 \pm 0.4$	8.5	Mortlock+13
1.50–2.00	$-1.19 \pm 0.06$	11.43	$7.5 \pm 1.2$	9.3	Mortlock+11 <sup>b</sup>
1.50–2.00	$-1.33 \pm 0.05$	$11.25 \pm 0.05$	$5.2 \pm 1.1$	9.0	Tomczak+14
1.50–2.50	$-1.45^{+0.06}_{-0.06}$	$11.32^{+0.13}_{-0.10}$	$3.1 \pm 0.7$	9.3	Kajisawa+09
1.80–2.20	$-1.34 \pm 0.07$	$11.22 \pm 0.14$	$3.1 \pm 0.6$	8.7	Fontana+06 <sup>a</sup>
2.00–2.50	$-1.56 \pm 0.06$	$11.24 \pm 0.10$	$1.7 \pm 0.4$	9.0	Mortlock+13
2.00–2.50	$-1.50 \pm 0.08$	11.43	$3.5 \pm 0.9$	9.4	Mortlock+11 <sup>b</sup>
2.00–2.50	$-1.43 \pm 0.08$	$11.35 \pm 0.13$	$2.6 \pm 0.9$	9.3	Tomczak+14
2.20–2.60	$-1.38 \pm 0.08$	$11.16 \pm 0.18$	$2.4 \pm 0.5$	9.0	Fontana+06 <sup>a</sup>
2.50–3.00	$-1.69 \pm 0.06$	$11.26 \pm 0.12$	$0.9 \pm 0.4$	9.3	Mortlock+13
2.50–3.00	$-1.74 \pm 0.12$	$11.57 \pm 0.33$	$0.4 \pm 0.4$	9.5	Tomczak+14
2.50–3.50	$-1.59^{+0.13}_{-0.14}$	$11.39^{+0.32}_{-0.20}$	$1.0 \pm 0.5$	9.5	Kajisawa+09
2.60–3.00	$-1.41 \pm 0.09$	$11.09 \pm 0.21$	$1.9 \pm 0.4$	9.2	Fontana+06 <sup>a</sup>
3.00–3.50	$-1.45 \pm 0.11$	$10.97 \pm 0.27$	$1.5 \pm 0.3$	9.4	Fontana+06 <sup>a</sup>
3.00–3.50	$-1.86^{+0.05}_{-0.04}$	$11.45 \pm 0.07$	$0.4 \pm 0.2$	10.4	Caputi+11
3.50–4.00	$-1.49 \pm 0.12$	$10.81 \pm 0.32$	$1.1 \pm 0.3$	9.6	Fontana+06 <sup>a</sup>
3.50–4.25	$-2.07^{+0.08}_{-0.07}$	$11.37 \pm 0.06$	$0.1 \pm 0.1$	10.4	Caputi+11
3.50–4.50	$-1.53^{+0.07}_{-0.06}$	$10.44^{+0.19}_{-0.18}$	$3.0^{+1.8}_{-1.2}$	8.5	Song+16
3.50–4.50	$-1.89^{+0.15}_{-0.13}$	$10.73^{+0.36}_{-0.32}$	$1.9^{+3.5}_{-1.3}$	8.5	Duncan+14
3.50–4.50	$-1.63 \pm 0.09$	$10.96 \pm 0.18$	$1.2 \pm 0.4$	8.5	Grazian+15
4.25–5.00	$-1.85^{+0.27}_{-0.32}$	$11.06 \pm 0.1$	$0.1 \pm 0.1$	10.5	Caputi+11
4.50–5.50	$-1.74^{+0.41}_{-0.29}$	$10.90^{+0.98}_{-0.46}$	$1.2^{+4.8}_{-1.2}$	8.7	Duncan+14
4.50–5.50	$-1.67^{+0.08}_{-0.07}$	$10.47^{+0.20}_{-0.20}$	$1.3^{+1.0}_{-0.6}$	8.7	Song+16
4.50–5.50	$-1.63 \pm 0.09$	$10.78 \pm 0.23$	$0.7 \pm 0.3$	8.7	Grazian+15
5.50–6.50	$-2.00^{+0.57}_{-0.40}$	$11.09^{+1.13}_{-1.06}$	$0.1^{+4.1}_{-1.1}$	9.0	Duncan+14
5.50–6.50	$-1.55 \pm 0.19$	$10.49 \pm 0.32$	$0.7 \pm 0.5$	8.9	Grazian+15
5.50–6.50	$-1.93^{+0.09}_{-0.09}$	$10.30^{+0.14}_{-0.15}$	$0.3^{+0.3}_{-0.1}$	9.0	Song+16
6.50–7.50	$-2.05^{+0.17}_{-0.17}$	$10.42^{+0.19}_{-0.18}$	$0.1^{+0.1}_{-0.5}$	9.2	Song+16
6.50–7.50	$-1.88 \pm 0.36$	$10.69 \pm 1.58$	$0.1 \pm 0.1$	9.2	Grazian+15

**Notes.** This table lists the parameters of the fitted Schechter functions that we use to carry out our calculations. These fits are all normalized to have the same Salpeter IMF with Pozzetti et al. (2007), Duncan et al. (2014), and Mortlock et al. (2015) originally using a Chabrier IMF, and Muzzin et al. (2013) using a Kroupa IMF.

<sup>a</sup> Fontana et al. (2006) fit the evolution of the Schechter parameters over redshift and not within individual redshift bins. These values are thus derived by using their fitting formula for the parameters and their associated errors.

<sup>b</sup> Mortlock et al. (2011) use a constant  $M^*$  at  $\log M^* = 11.43$  across the redshift range they study from  $z = 1$ –3.



exception of Grazian et al. (2015) whose results lead to a slightly lower value of  $\phi_T$ .

### 3.1.1. Integrating the Stellar Mass Function

The major aspect of this paper is that we integrate the fitted Schechter function for all of the mass function data below the limit in which the data is obtained. There are two distinct questions concerning doing this. One is that if we are using fits from mass functions in which the data is not as deep as others, then are we technically able to retrieve the mass function correctly? As the number density depends strongly upon the value of the faint-end slope  $\alpha$  (Section 3.2) we can express this question another way: if we have data down to some limit, say  $M^*$ , and fit the Schechter parameters, will we retrieve the same parameters if we were probing down to a low mass limit?

The other issue, which we address in the next subsection, has to do with how low we should integrate these mass functions. Here we discuss the more technical point of whether or not the Schechter function can be extrapolated at all with fits that are based on a variety of mass functions of diverse depths.

We address this issue in a few ways. We first show in Figure 1 the mass functions we use as a function of redshift. The dashed black lines show the extrapolation we use down to our  $M_* = 10^6 M_\odot$  limit. We show in Figure 2 the fitted  $\alpha$  values for these mass functions as a function of the depth of the data, parameterized by how deep the data is in reference to the fitted  $M^*$  values. As can be seen, we do not probe as deep at higher redshift. We also see a trend, well established now in several papers (e.g., Duncan et al. 2014; Song et al. 2016), that the value of the fitted  $\alpha$  becomes steeper at higher redshifts. There is a slight trend such that the fitted value of  $\alpha$  becomes more steep (i.e., more lower mass galaxies) for deeper data, although this is not present at the highest redshifts.

We also carry out two different simulations to demonstrate that we are able to retrieve the correct value of  $\alpha$ , and the other Schechter function parameters,  $M^*$  and  $\phi^*$ , if we are probing about a factor of 10 less massive than  $M^*$ , or deeper. Figure 3 shows the results of these simulations.

The first one on the top panel of Figure 3 shows a full refitting of the lowest redshift ( $z \sim 4$ ) mass functions from Duncan et al. (2014). These fits were redone using the emcee MCMC code (Foreman-Mackey et al. 2013). The resulting fits thus technically differ from those in Duncan et al. (2014), most significantly in the marginalized errors that are slightly smaller, but not in a significant way. The dashed vertical line shows the value of  $M^*$  for this mass function when fit at its deepest level down to the  $M_* = 10^{8.5} M_\odot$  limit, which is a factor of 100 times less massive than the value of  $M^*$ . The blue points show the value of the refitted  $\alpha$  values of the Schechter function as a function of depth. As can be seen, within 0.5 dex of  $M^*$  the mass function is difficult to fit correctly, providing an incorrect  $\alpha$  or one with a large error bar. However, when the depth of the data is larger than 0.5 dex from  $M^*$  we obtain an accurate measure of  $\alpha$ .

The bottom plot of Figure 3 shows a simulation whereby all of the mass functions we use were resampled to end at 1/10th the value of  $M^*$  (1 dex in log space) and then fitted with the resulting faint-end slope,  $\alpha_{\log M^* - 1}$ . As shown in Figure 2, all of our mass functions are complete to 1/10 the value of  $M^*$  or deeper. These simulated mass functions take into account the number of galaxies present in each bin, and therefore also the

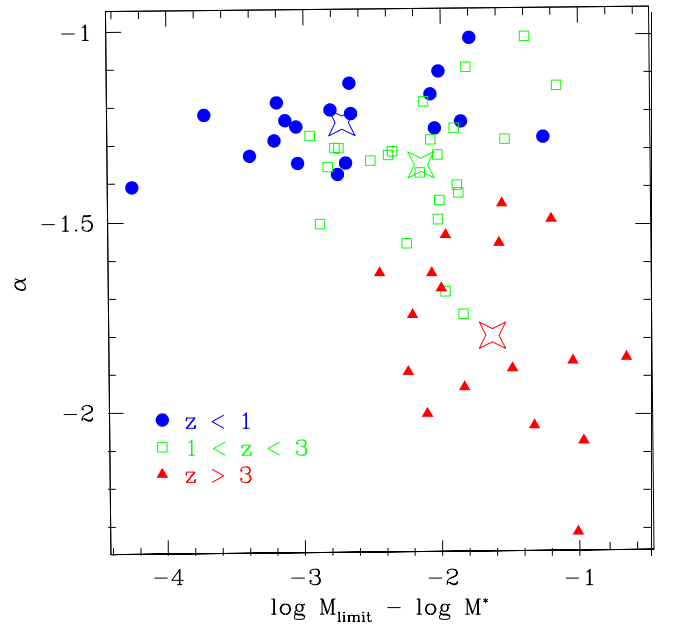


**Figure 2.** Relationship between the fitted value of  $\alpha$  and the depth of the data in which the mass function was fitted in reference to the value of  $M^*$  (see text). Systems that are more negative in  $\log M_{\text{limit}} - \log M^*$  have deeper observed mass functions with the deepest data at  $z < 1$  probing a mass limit that is a factor of  $10^4$  lower than  $M^*$ . The colors of the points denote the redshift range, with the blue circles those galaxies at  $z < 1$ , the green boxes those at  $1 < z < 3$ , and the red triangles those at  $z > 3$ . The large open stars show the average values within each redshift range.

statistical uncertainty when dealing with smaller numbers of galaxies.

We then compare this simulated value with the full mass range fitted value  $\alpha_{\text{FULL}}$ , which probes to the depths shown in Figure 2. This difference is plotted as a function of the full value  $\alpha_{\text{FULL}}$  in Figure 3. This shows that as a function of redshift, and the shape of the mass function as parameterized by  $\alpha_{\text{FULL}}$ , the value of  $\alpha$  can be easily retrieved when the depth of the mass function is at least 1/10th the value of  $M^*$ . This holds as well for the other Schechter function parameters. We therefore use only those mass functions that are at least a factor of 10 deeper than their fitted  $M^*$  value (Figure 2).

We must also consider the effects of the covariances between  $M^*$ ,  $\phi_T$ , and  $\alpha$  when these parameters are fitted together. The resulting values of these parameters are correlated, as can be seen in their distributions from various mass function fits (e.g., Fontana et al. 2006; Grazian et al. 2015; Weigel et al. 2016). For example, the best-fitting values of  $\alpha$  can be strongly affected by a few galaxies at the massive end of the mass function, which should in principle have little effect on the low-mass slope, but when fitting can. This covariance is such that there is a strong correlation between the values of  $\alpha$ ,  $\phi^*$ , and  $M^*$  such that the value of  $\alpha$  becomes more negative as  $M^*$  increases, and  $\phi^*$  goes up when  $M^*$  does down. This is such that a higher fitted  $M^*$  increases the resulting value of  $\phi_T$ , and a more negative  $\alpha$  does so as well; therefore, the covariance between these is a potentially serious issue. However, as there is a corresponding drop in the value of  $\phi^*$  when  $M^*$  increases, this negates to some extent the strong covariance between  $\alpha$  and  $M^*$ .

The mass function fitting we use does not often provide the covariance between these parameters in the respective results

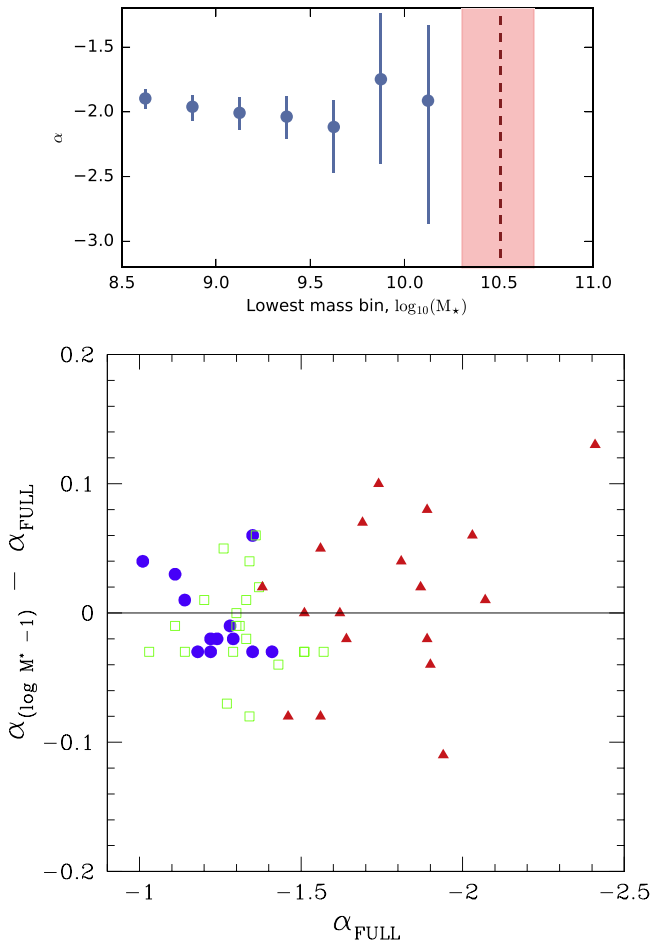


**Figure 3.** Two panels on this figure show our simulations and determinations based on actual data for how the faint-end slope  $\alpha$  changes as a function of depth relative to the value of  $M^*$ . In the top panel we show an example using the  $z \sim 4$  mass function from Duncan et al. (2014) that reaches a nominal depth of  $\log M_* = 8.5$ , which is 100 times deeper than the value of  $M^*$  at this redshift. The vertical dashed line shows this value of  $M^*$ , and the shaded pink area shows the 1-sigma errors on the full  $M^*$  fit, which are the 16 and 84 percentiles in the marginalized distribution, with the best-fit dashed line being the 50th percentile of this distribution. Mathematically this is  $\log M^* = 10.50^{+0.19}_{-0.17}$ . The blue points show the retrieved value of  $\alpha$  when redoing the entire Schechter function fits, but only to the quoted mass depth on the  $x$ -axis. This fitting is done through a full  $V_{\max}$  methodology as outlined in Duncan et al. (2014) and in the text. The bottom panel shows the difference between the fitted  $\alpha$  values when using the full depth of the data ( $\alpha_{\text{FULL}}$ ), and when only fitting down to a mass limit of  $\log M^* - 1$  ( $\alpha_{(\log M^* - 1)}$ ). Every mass function we use in this paper is shown here. The colors denote the redshift range, as in Figure 2. As can be seen, we are able to retrieve the values of  $\alpha$  as long as we can reach at least 1/10 the value of  $M^*$ . The other Schechter function parameters are also accurately retrievable in these simulations.

we use. The error bars on the fits, however, do represent a good representation of the extent of the range of  $\phi_T$ , when combined together. That is, the error on  $\phi_T$  is calculated by taking the extent of the error bar when  $\alpha$  is at its maximum negative extent,  $M^*$  is at its highest value, and  $\phi^*$  is at its lowest value for an upper error limit, and vice versa for the lower error limit.

We investigate the total effect of this covariance by simulating the covariance for the  $z = 4$  mass function from Grazian et al. (2015). We show the distribution of  $\phi_T$  values when we randomly sample 1000 times across the covariance of the Schechter function fitting parameters in Figure 4. The distribution of  $\phi_T$  is not Gaussian, but has a tail at higher values of  $\phi_T$ . However, the average value of this distribution,

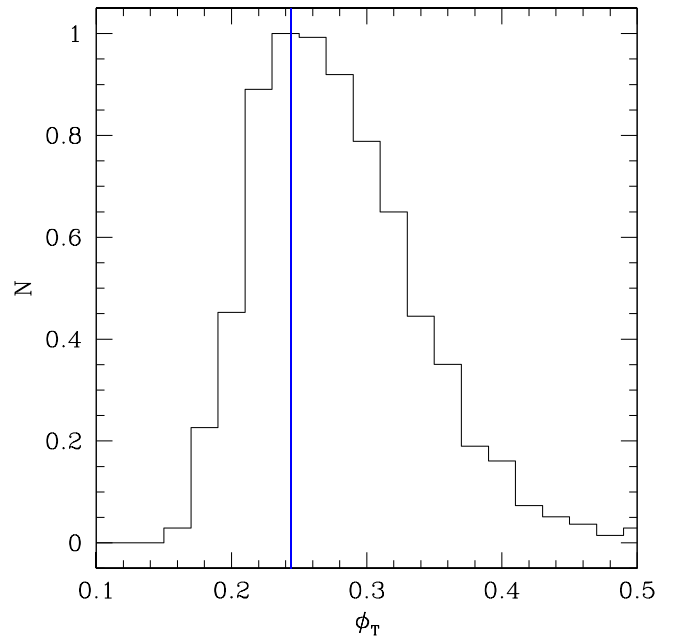


**Figure 4.** Relative distribution of  $\phi_T$  values derived from the sampling of the covariance between the parameters of  $\alpha$ ,  $\phi^*$ , and  $M^*$  for one of the mass functions used at  $z = 4$  from Grazian et al. (2015). The average value of the distribution is  $\phi_T = 0.27$ , which is close to the derived value of  $\phi_T = 0.24$ , which is shown by the vertical blue line. The range here is also similar to the resulting errors we calculate for  $\phi_T$ .

$\phi_T = 0.27$ , is just slightly higher than the value calculated with the best-fit Schechter values, which is  $\phi_T = 0.24$ . The error range calculated with our method is also similar to the distribution of these points. Other covariance analyses result in similar conclusions.

### 3.1.2. The Galaxy Stellar Mass Lower Limit

Another main issue with these mass functions is how deep to integrate to obtain the total number density of galaxies at a given redshift. Our choice here is important, as the total number can depend significantly on the limits used in the integration. Our initial and fiducial low-mass limit is  $M_* = 10^6 M_\odot$ , which is the typical lower limit for dwarf galaxies in the nearby universe. Most systems at masses lower than this are star clusters within galaxies, or debris from galaxy interactions. For example, many of the galaxies in the Local Group and nearby clusters with masses lower than this are likely either of tidal origin, or are misidentified star clusters (e.g., Penny & Conselice 2008; Ibata et al. 2013).

While there are certainly some galaxies at lower masses than this in the local universe, by using a  $M_* = 10^6 M_\odot$  limit we limit our exposure to the risk of extrapolating the mass function too deeply. Because of the use of a limit whereby we are probing beyond the direct observations, we cannot be 100% certain that the mass function is necessarily valid to these depths. Also, the exact value of this lower limit will drive the quantitative values of our total number density strongly. Therefore the nominal total number density we calculate is based on the number of galaxies greater than  $M_* = 10^6 M_\odot$ . We also assume that the mass functions of high-redshift galaxies do not change slope at lower mass limits than we currently probe. If they do so, then our results would be different. However, for the reasons given above, and below,

this change in slope is unlikely as this change in mass function shape at low masses has not been seen at any redshift including at lower redshift where we can probe deeper than at higher redshift.

We also justify using these mass limits, and thus extrapolating our mass functions down to  $M_* = 10^6 M_\odot$ , in other ways. While this paper has nothing directly to say about reionization, many authors have shown that an extrapolation of the mass function to at least this mass limit is needed to reionize the universe. As shown in papers such as Robertson et al. (2015), Duncan & Conselice (2015) and Dufy et al. (2014), the integration of the measured mass function at  $z \sim 7$  to at least this  $M_* = 10^6 M_\odot$  limit is necessary and sufficient to reionize the universe. While this does not imply that these galaxies are reionizing the universe, it does show that this limit is required if UV emission from galaxies is the ionization culprit. This is also consistent with recent determinations of the cosmic background light which show that there are a factor of 10 more galaxies than we can presently observe, per unit area, needed to account for this light (e.g., Mitchell-Wynne et al. 2015).

Furthermore, predictions of Cold Dark Matter show that the luminosity and mass functions of galaxies should be very steep with a mass function slope of  $\alpha \sim -2$  (e.g., Jenkins et al. 2001), it is thus reasonable to assume that measured luminosity and mass functions continue to increase past the arbitrary observational limit we can reach with observations today. Furthermore these theoretical models show that there are indeed galaxies down to these low masses, both through dark matter halos and through simulated galaxies (e.g., Jenkins et al. 2001; Gonzalez-Perez et al. 2014; Henriques et al. 2015).

Furthermore, the stellar populations of low-mass galaxies in the local universe show that many of the stars in these galaxies were formed at very early times, and thus were present at these high redshifts (e.g., Grebel et al. 2003), and that by examining the mass function of Local Group galaxies we also obtain a high number of low-mass systems with a retrieved steep  $\alpha$  value (e.g., Graus et al. 2015). We however later test how our results would change if we were to use a different observational limit to constrain this uncertainty.

### 3.2. Integrated Number Density Evolution

We integrate the fitted Schechter parameters for the various fits to the mass functions given in the papers described in the previous section to obtain a measurement of the total number densities of galaxies.

We calculate at a given redshift bin the total number density of galaxies ( $\phi_T$ ), given the parameters of the Schechter fit to the mass function,  $\phi(M, z)$ :

$$\phi_T(z) = \int_{M_1}^{M_2} \phi(M, z) dM. \quad (2)$$

A good approximation for this integral into an analytical formula can be obtained by taking the approximation for the Schechter function when the stellar mass limit is low. The formula for this is given by

$$\phi_T(z) \approx \frac{-\phi^* 10^{(\alpha+1)(M_2-M_*)}}{(\alpha+1)}, \quad (3)$$

showing that the number density is a function of all the Schechter function parameters, but is especially dependent on the value of  $\alpha$ , and the lower limit to integration  $M_2$ . However,

throughout this paper we do not use this approximation, but carry out direct numerical integration of Equation (2).

When we plot the integrated number density  $\phi_T$  (Figure 5) for each data point from our various studies we find some differences at the same redshift between the surveys for calculating the total number density from  $M_1 = 10^6 M_\odot$  to  $M_2 = 10^{12} M_\odot$ . We find a general increase with redshift in the integrated number density, although some studies, such as Perez-Gonzalez et al. (2008), find a slight decline from  $z = 0$  to  $z = 4$ . On the other hand, studies that are based on very deep near-infrared imaging, such as Kajisawa et al. (2009), Caputi et al. (2011), and Mortlock et al. (2011, 2015) find an increase with redshift in  $\phi_T$  with higher redshift. This is due to the fact that the fitted  $\alpha$  values are steeper at higher redshifts in these studies. More recent results also find a steep  $\alpha$  at high redshifts, which provides a large value of  $\phi_T$ , including Tomczak et al. (2014), Duncan et al. (2014), Grazian et al. (2015), and Song et al. (2016).

A steep  $\alpha$  value continues to be found in preliminary mass functions of even deeper studies utilizing lensing from the Hubble Frontier Fields (Laporte et al. 2015) and the deepest *HST* field data, with  $\alpha$  values approaching or exceeding  $\alpha = -2$  (e.g., Bouwens et al. 2015; Livermore et al. 2016). Thus, there are more low-mass galaxies per massive galaxy at high redshifts than in the local universe.

We summarize these results and their errors in Figure 5. Note that the integration of the quantity, given in Equation (2) and plotted here, shows that, while there are generally more galaxies at higher redshift, the exact number has some variation. From Figure 5 it is however clear that there is a rapid increase in  $\phi_T$  up to  $z = 3$  with a more mild increase at higher redshifts.

We also show in Figure 5 in the left panel the number densities of galaxies down to the limit of integration, which matches the completeness of each point in the original data. This is shown as the small points just below the main data points, which have error bars. This shows that our extrapolations to the lowest mass limits are largest for the highest redshift galaxies by sometimes a factor of 10 or so, and much less at lower redshifts.

When we fit the relation of  $\phi_T$  as a function of time we find that the relationship between the total number density  $\phi_T$  and time ( $t$ ) is such that the increase is slower at lower redshift  $z < 1$  than at higher redshift. This shows that there is a rapid increase in the number of galaxies in the universe above our nominal threshold of  $M_* = 10^6 M_\odot$ . The formal fit with time is

$$\log \phi_T(t) = (-1.08 \pm 0.20) \times \log(t) - 0.26 \pm 0.06, \quad (4)$$

where  $t$  is the age of the universe in units of Gyr. This equation shows that the number of galaxies in the universe declines with time, with an overall decrease that goes as  $\sim 1/t$ . We find that a fit with time can be parameterized well in this way, although a fit with redshift does not produce a single well-fitted function. We also show in Figure 6 the change in the number densities of galaxies as a function of co-moving volume, showing that the majority of the galaxies in the universe are in the early universe. This also shows likewise that the average total number density of galaxies declines as time goes on.

We also show in Figure 7 the number density evolution at higher mass limits of  $M_* = 10^7 M_\odot$ , and at  $M_* = 10^{10} M_\odot$ . We find a few things when examining these results at different masses. First it appears that there is a turnover in the evolution

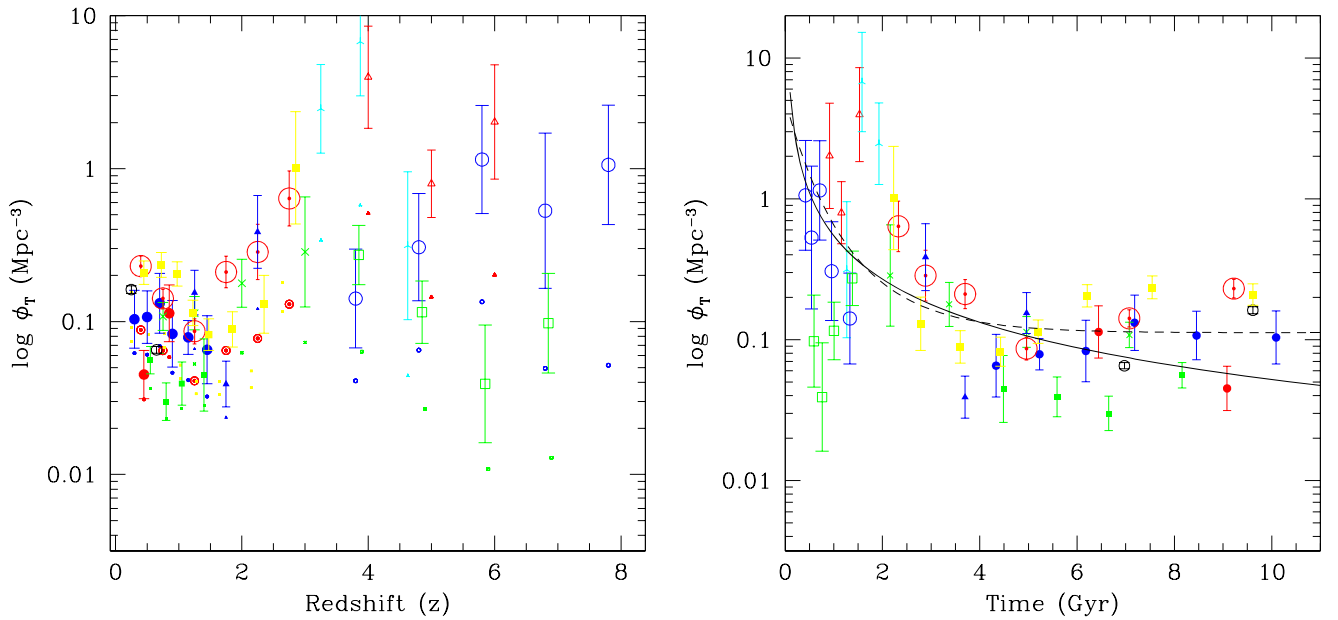


**Figure 5.** Figure showing the evolution of the co-moving total number densities for galaxies within the universe as a function of both redshift and time. Shown here are the various surveys that are used in these measurements. This includes measurements from Perez-Gonzalez et al. (2006; blue solid circles at  $z < 2$ ), Fontana et al. (2004; large solid red circles at  $z < 1$ ), Kajisawa et al. (2009; green crosses at  $z < 4$ ), Mortlock et al. (2015; large red open circles at  $z < 4$ ), Muzzin et al. (2013; black squares at  $z < 1$ ), Pozzetti et al. (2007; green boxes at  $z < 2$ ), Mortlock et al. (2011; blue triangles at  $z < 4$ ), Caputi et al. (2011; cyan up arrows at  $z \sim 4$ ), and Tomczak et al. (2014; solid yellow squares at  $z < 3$ ). For the higher redshift points we use the mass functions from Duncan et al. (2014; red triangles at  $z > 4$ ), Song et al. (2016; blue open circles at  $z > 4$ ), and Grazian et al. (2015; green open boxes at  $z > 4$ ). The smaller symbols without error bars, usually toward the bottom of the plot on the left panel, show the integrated values for each mass function to the completeness limit reached by each survey. The solid line in the right panel is the best fit to the relation of  $\phi_T$  with time, while the dashed line is the merger model best fit discussed in Section 4.3.

of  $\phi_T$ , such that for massive galaxies there is a step increase in the number density of galaxies above the limit of  $M_* = 10^{10} M_\odot$ . This is opposite to what we find when we examine the evolution at the limit of  $M_* = 10^6 M_\odot$ . This turnover occurs at roughly  $M_* = 10^7 M_\odot$ , as shown in Figure 7. This demonstrates that at this limit the evolution of  $\phi_T$  is nearly constant with redshift.

The implication for these results are discussed in the next section. Overall, we are now able to use these results to determine how many galaxies are in the observable universe with our various mass limits and the likely methods by which galaxies are evolving in number density, as well as the implications for background light in the optical and near-infrared based on these results.

#### 4. IMPLICATIONS

The major result from this paper is that we now have a scientific measurement of the evolution of the total galaxy number density up to  $z = 8$ . We investigate several implications for these results, including the total number of galaxies in the universe, galaxy evolution, extragalactic background light, Olbers' paradox, and future galaxy surveys.

##### 4.1. Comparison to Theory

One of the things we can do with this analysis of evolving number densities is to compare our result to those of theory. Recently, the Illustris simulation derived the number densities of galaxies as a function of redshift (Torrey et al. 2015). The Illustris simulation is a cosmological hydrodynamical simulation designed to probe galaxy formation processes using a periodic box of size  $L = 106.5 \text{ Mpc}$ . The overall setup and code is described in Vogelsberger et al. (2014), but in summary

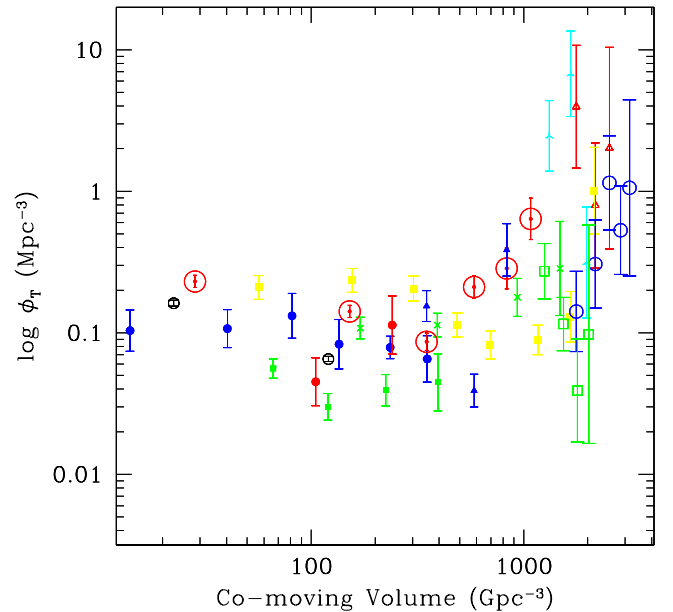


**Figure 6.** Similar to Figure 5 but showing the change in total galaxy number density as a function of total co-moving volume out to a given redshift. This total galaxy density increases with larger volume as  $\text{Vol}^{1.28 \pm 0.38}$ . The symbols are the same as Figure 5. This figure shows that the majority of the galaxies in the currently observable universe are at high redshift.

includes hydrodynamics, gravity, star formation with feedback, and radiative cooling. It does a reasonable job of matching observations of the galaxy population (e.g., Genel et al. 2014).

Here we compare directly with the predictions for the number of galaxies above a certain mass, or the cumulative number density of galaxies, which is exactly what we have discussed earlier in this paper. Torrey et al. (2015) provide an



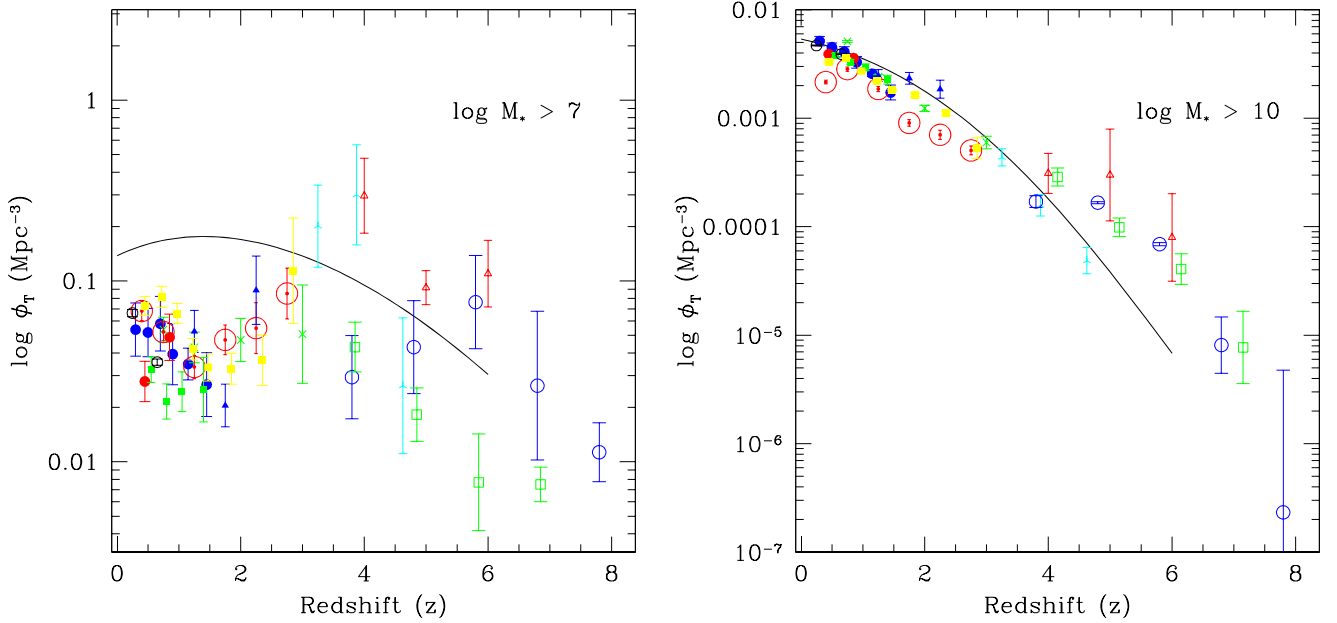


**Figure 7.** The number density evolution for galaxy selection with differing mass limits than those given in Figure 5. In the left-hand panel we show the evolution of galaxies down to a limit of  $M_* = 10^7 M_\odot$ , while on the right-hand side we show the evolution for a limit of  $M_* = 10^{10} M_\odot$ . The solid lines in both panels show the predicted number density evolution as parameterized by Torrey et al. (2015). Note that the masses quoted here are those calculated with a Chabrier IMF to match the Torrey et al. (2015) models. The symbols and shapes of the points denote the same survey as described in Figure 5.

analytical formula with which to compare our values. However, up to our redshifts of interest, these are only provided down to  $M_* = 10^7 M_\odot$  using a Chabrier IMF. We thus compare our integration down to this mass limit with these models in Figure 7. We also convert our number densities to this IMF before comparing with the Torrey et al. (2015) results. We also compare with a higher mass limit of  $M_* = 10^{10} M_\odot$ . This comparison is shown in Figure 7 for these two mass limits.

What can be seen in these figures is that the cumulative number density observed agrees reasonably well with the predictions for the highest mass galaxies at  $M_* > 10^{10} M_\odot$ , but does not do as well of a job at the lower mass limits. The reason for this is that the low-mass end of the mass function, particularly at lower redshifts, does not match the data, with the theory values being too high. Interestingly, this does not seem to be the case at higher redshifts where the theory and data agree better. The reason for the disagreement at low redshift is likely due to the fact that the data show increasingly shallow values of  $\alpha$ , the faint-end slope, compared to the simulation. This comparison also shows that our extrapolation down to low mass limit is not excessive as we are still below what is predicted in theory. Later in the next section we discuss the likely cause of this changing  $\alpha$  value and why the total number of galaxies declines with time.

#### 4.2. The Total Number of Galaxies in the $z < 8$ Universe

The total number of galaxies in the universe is an interesting scientific question, although it may not reveal anything fundamental about the cosmology or underlying physics of the universe. Nonetheless, it is an interesting number that should be known and quantified, although expressing it has to be done within certain constraints.

We use the results from Section 3 to investigate the total number of galaxies in the currently observable universe down to a mass limit of  $M_* = 10^6 M_\odot$  in two different ways. We

explore other limits that give different answers later. The first is through simply taking the average total number of galaxies  $\phi_T$  at a given redshift in Figure 5 and calculating its scatter. When multiplied by the volume at that redshift bin, this gives us the average total number of galaxies within that volume, which uses all the available data. Then we calculate the total number as simply the sum of these average numbers at each bin. When we do this calculation we find that the total number of galaxies is given by

$$N_{\text{tot,obs}} = 2.8 \pm 0.6 \times 10^{12}$$

up to  $z = 8$ , which is almost a factor of 10 larger than what is obtained from direct counts from the deepest optical/near-infrared imaging data, as described in the Appendix.

To obtain another estimate of the total number of galaxies in the currently visible universe down to  $M_* = 10^6 M_\odot$ , we integrate Equation (4) from  $0 \leq z \leq 8$  using our best-fit relation. This avoids having to use a single measurement of the mass function to obtain a result, and as such our measurement is based on all the available data. Because the mass functions we use are taken from a variety of fields, we are also accounting for cosmic variance within our measurements. To calculate the maximum and minimum limits to our total count, we take into account the errors assigned to  $\phi^*$ ,  $\alpha$ , and  $M^*$ .

We use the fit above to calculate the total number of galaxies within the currently visible universe down to  $M_* = 10^6 M_\odot$  from  $z_1 = 0$  to  $z_2 = 8$ , which is an integral over the number densities  $\phi_T(z)$  and volume:

$$N_{\text{tot,fit}} = \int_{t_1}^{t_2} \int_0^{4\pi} D_H \frac{(1+z)^2 D_A^2}{E(z)} \phi_T(t) d\Omega dt \quad (5)$$

$$N_{\text{tot,fit}} = (1.2^{+0.4}_{-0.2}) \times 10^{12}. \quad (6)$$

where the volume is integrated over the entire sky through  $4\pi$  in steradians and  $D_A$  is the angular size distance,  $D_H = c/H_0$ ,

and  $E(z) = (\Omega_M(1+z)^3 + \Omega_\Lambda)^{1/2}$ . Thus knowledge of the redshift and the time since the Big Bang are required to perform this integration.

Performing this integral to  $z = 8$  gives us 1.2 trillion individual galaxies, which again is just less than a factor of 10 times higher than the number of galaxies, which in principle can be observed today in the universe with present technology (see [Appendix](#)). We use the difference between this value of the total number of galaxies and that calculated with the average  $\phi_T$  values above to obtain a most likely value for the average number of galaxies. As both methods are equally valid measurements, we take the average between them. This gives us the ultimate final value of the total number of galaxies within the currently visible universe down to  $M_* = 10^6$  ( $N_{\text{tot,final}}$ ),

$$N_{\text{tot,final}} = (2.0^{+0.7}_{-0.6}) \times 10^{12}. \quad (7)$$

This large value implies that there is a vast number of galaxies that we have yet to discover at magnitudes fainter than  $m_{\text{max}} \sim 29$  as we discuss in [Section 4.4](#).

However, as mentioned, this number depends strongly upon our use of a limit of  $M_* = 10^6 M_\odot$ , and our redshift limit of  $z = 8$ . It is important to explore how the total number would change if these limits were different. We find that the total number does not depend much on the redshift limit. If we extend our study to  $z = 12$  by using the same number densities we find at  $z = 8$ , our observational limit, then we find slightly more galaxies with the total number increasing by 65%. There may be very few galaxies at redshifts higher than this.

In terms of the mass limit, there is more of a difference when using a lower limit. While we have argued earlier that the mass limit of  $M_* = 10^6 M_\odot$  is a natural one for galaxies, it is important to discuss how the total number would change if we used a different stellar mass limit. If we use a factor of 10 smaller limit of  $M_* = 10^5 M_\odot$ , we find roughly a factor of  $\sim 7$  more galaxies than using the  $10^6 M_\odot$  limit. Thus our limit in [Equation \(7\)](#) is actually a lower limit both in terms of the mass limit and redshifts. The end result of this is that there are at least  $2 \times 10^{12}$  (two trillion) galaxies in the currently visible universe, the vast majority of which cannot be observed with present-day technology as they are too faint.

#### 4.3. Galaxy Evolution through Mergers and Accretion

One of the major results we find is that the total number density of galaxies in the universe declines with time from high to low redshift when using a  $M_* = 10^6 M_\odot$  limit. In fact, what we find is that measured mass functions down to a limit of  $M_* = 10^6 M_\odot$  give a total number density that declines by a factor of 10 within the first 2 Gyr of the universe's history, and a further reduction at later times. This decline may further level off between redshifts of  $z = 1$  and  $z = 2$ . The star formation rate during this time is also very high for all galaxies, which should in principle bring galaxies, which were below our stellar mass limit into our sample at later times. This would naturally increase the number of galaxies over time, but we see the opposite. This is likely due to merging and/or accretion of galaxies when they fall into clusters that are later destroyed through tidal effects, as no other method can reduce the number of galaxies above a given mass threshold.

We can use a straightforward argument to demonstrate that hierarchical galaxy formation must be occurring in the universe

over time at this stellar mass limit. The first way we argue this is to calculate the number of galaxies in the nearby universe, and then infer the total number we would observe up to  $z = 8$  if the co-moving number densities of galaxies remained the same. We then compare this with the total number of galaxies we can observe within the UDF-Max itself (see [Appendix](#)).

Using the number densities from the GAMA survey ([Baldry et al. 2012](#)), and by assuming a homogeneous universe, we find that there would be  $\sim 2.8 \times 10^{11}$  galaxies at  $z < 8$ . If we use the inferred total number from [Equation \(7\)](#), then there are  $\sim 7$  times more observable galaxies than what we would predict in the universe if it had the same number density as in the local universe. There is likely no other way to remove these galaxies except through merging, destruction, or accretion with other systems.

We investigate this further with a simple merger destruction model whereby when an individual merger or destruction event occurs, the number of galaxies within a volume decreases by one. Thus if there are  $N_m$  mergers per unit volume per unit time, then the number density declines by  $N_m$  galaxies in that volume, and over that time period.

We parameterize this overall merger rate in units of the number of mergers per unit volume per unit time as an exponentially declining function:

$$R(t) = R_0 e^{-t/\tau} \quad (8)$$

where  $R_0$  is the merger rate in units of number of mergers per Gyr per  $\text{Mpc}^3$  at  $z = 0$ , and  $\tau$  characterizes the global merger timescale. In this characterization the number of mergers per unit volume, which occur within a given redshift, or time, interval between time  $t_1$  and  $t_2$ , which is equivalent to a number density ( $\phi_T$ ) change, is given by

$$\phi_T(t_1) - \phi_T(t_2) = \int_{t_1}^{t_2} R_0 e^{-t/\tau} dt = R_0 \tau (e^{-t_1/\tau} - e^{-t_2/\tau}). \quad (9)$$

If we measure this from  $t_1 = 0$ , then the total integrated decline in the number density  $\phi_T(t)$  is given by

$$\phi_T(t) = \phi_T(0) - R_0 \tau \times (1 - e^{-t_2/\tau}) \quad (10)$$

where  $\phi_T(0)$  is the initial total number densities for galaxies at high redshift.

If we then use the observed data from [Figure 5](#), and set  $\phi_T(z = 8) = n_0 = 0.7 \text{ Mpc}^{-3}$ , then we find that the best-fitting parameters of this merger model are  $R_0 = 1.28 \pm 0.20$  mergers  $\text{Gyr}^{-1} \text{Mpc}^{-3}$ , and  $\tau = 1.29 \pm 0.35$  Gyr. This model further predicts that at  $z = 1.5$  the merger rate is  $R \sim 0.05$  mergers  $\text{Gyr}^{-1} \text{Mpc}^{-3}$ . This compares well with the directly derived merger rates from [Conselice \(2006\)](#), who find that the merger rate for  $M_* > 10^8 M_\odot$  galaxies is  $R \sim 0.03$  mergers  $\text{Gyr}^{-1} \text{Mpc}^{-3}$ , while for  $M_* > 10^9 M_\odot$  galaxies the rate is  $R \sim 0.01$  mergers  $\text{Gyr}^{-1} \text{Mpc}^{-3}$ . These are also close to the values found by [Lotz et al. \(2011\)](#) for more massive mergers using an independent method, and to [Bluck et al. \(2012\)](#) who look at minor merger pairs.

One caveat of this comparison, however, is that the merger rate we infer from the decrease in number densities in no way reveals what type of mergers these galaxies were involved with. They could be in minor mergers with much more massive galaxies, or major mergers with galaxies of similar masses. The comparison with [Conselice \(2006\)](#) is for a specific type of

merger—major mergers with mass ratios of 1:4 or higher. However, the merger rate we derive from the evolution in number density is higher than the major merger rate from Conselice (2006), and this is likely due to the increase presence of minor mergers for these systems. In fact, we find that the merger rate goes up by about a factor of two for minor mergers (Bluck et al. 2012) at  $z < 3$ , suggesting that this is indeed the reason for the difference. Overall, however, this argument demonstrates that a merger interpretation is tenable given the similarity of merger rates derived using two very different ways to measure the merger history.

Also, we find from Figure 7 that the number density evolution turns over for higher mass limits and in fact begins to increase with time for limits  $M_* > 10^7 M_\odot$ . This implies that the majority of the merging occurs at the lower mass range.

The major conclusion from this is that galaxy merging and accretion/destruction is the likely method in which lower mass galaxies decline in number densities through cosmic time. As discussed in, e.g., Conselice (2014), this is also a major way in which galaxy formation occurs at these epochs. However, we have a limited amount of information concerning the merging history at  $z > 3$  (e.g., Conselice & Arnold 2009), yet some results show that the merger history may be even more important at higher redshifts  $1 < z < 3$  than at lower (e.g., Ownsworth et al. 2014) and this may extend to even higher redshifts.

#### 4.4. Background Light and Olbers' Paradox

One of the implications for our results is that there should be a significant number of galaxies in the universe, which with current technology we cannot observe, even within deep *HST* images. This naturally leads to the issue of background light in the universe in the observed optical, as well as other problems such as Olbers' paradox, or scientifically understanding why the sky is mostly dark at night.

We do not give a detailed scientific discussion of the background light issue, as understanding the contributions of galaxies, as well as an absolute measurement of the background light in the optical, is still controversial and difficult to measure (e.g., Bernstein 2007; Dominguez et al. 2011; Mitchell-Wynne et al. 2015). What we can do, using the results of this paper, is discuss how many galaxies there are per unit area of the sky and what this implies about these background light observations.

First, using our final value of  $N_{\text{tot,final}}$ , we calculate that the projected density across all redshifts is on average 10,000 galaxies per arcmin<sup>2</sup>, which corresponds to an average of  $\sim 3$  galaxies per arcsec<sup>2</sup>. Using these numbers we can determine what fraction of the sky should be covered by galaxies. If we take the hypothesis that these 3 per arcsec<sup>2</sup> galaxies occupy all the area on the sky, this gives an average size for these galaxies of 0.32 arcsec in radius. This is similar to the effective radii found for the faintest galaxies in deep *HST* imaging, including the GOODS fields (e.g., Bouwens et al. 2004; Ferguson et al. 2004), as well as deeper imaging from *HST* WFC3 (Ono et al. 2013) for the highest redshift systems. If the average galaxy is larger than 0.32 arcsec, then it is certain that every part of the sky is occupied by part of a galaxy with stellar masses  $M_* > 10^6 M_\odot$  at  $z < 8$ . Thus, it appears that there are enough galaxies to nearly cover the entire sky when using a  $10^6 M_\odot$  limit. If we were to use a lower integration limit such as  $10^5 M_\odot$ , the number of galaxies in the sky increases by a factor

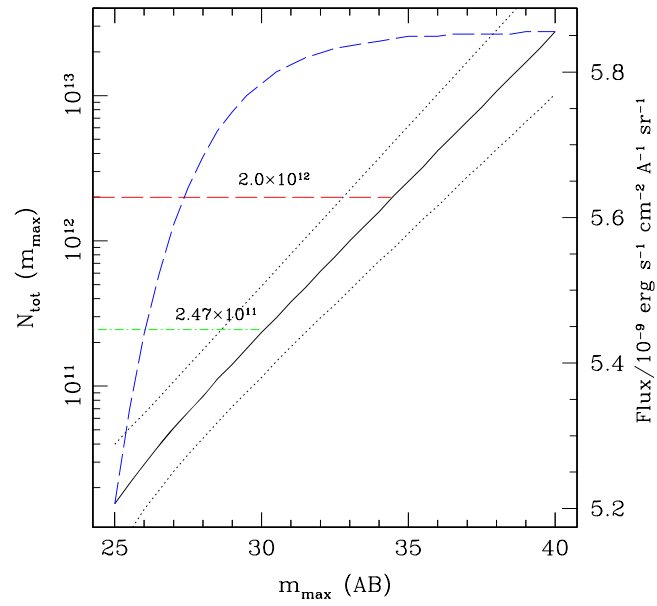


**Figure 8.** Plot showing the integrated number of galaxies as a function of magnitude (solid black line and errors as dotted lines), and the integrated flux density of galaxies in units of  $10^{-9} \text{ erg s}^{-1} \text{ cm}^{-2} \text{ \AA}^{-1} \text{ sr}^{-1}$  as a function of magnitude (blue dashed line). The two dashed horizontal lines show the observed total number of galaxies we can currently potentially observe with present-day technology (green dot-dashed) and the predicted total number at  $z < 8$  based on integrated stellar mass functions (red dashed).

of  $\sim 7$ , making it nearly certain that all parts of the sky would be covered.

This demonstrates that, on average, every point in the sky should contain part of a galaxy in principle. Most of these galaxies are, however, at higher redshifts, with the majority (around two-thirds) at  $z > 5$ , with the corresponding surface density of galaxies  $\sim 0.8 \text{ galaxies arcsec}^{-2}$  at  $z < 5$ . Since most galaxies are extremely faint and cannot be easily observed with today's technology, we can only detect the presence of these galaxies through the cosmic background light (e.g., Bernstein 2007; Dominguez et al. 2011).

Using the number of galaxies per magnitude and the magnitude limit that would exist for a total number given in Equation (7) we calculate the total flux density per steradians in the sky (Figure 8) as a function of magnitude. We do this by using the results in the Appendix, where we calculate the distribution of galaxy magnitudes in the UDF. From this we calculate the total flux density by integrating the flux density from each magnitude down to some magnitude limit.

Figure 8 shows that at magnitudes around 30, and fainter, we find an integrated flux value  $\sim 5.8 \times 10^{-9} \text{ erg s}^{-1} \text{ cm}^{-2} \text{ \AA}^{-1} \text{ sr}^{-1}$ . This value does not increase very much at fainter magnitudes. This flux compares well with the limits on the optical background from, e.g., Bernstein (2007) who finds an optical background value in the *I* band of  $7 \pm 4 \times 10^{-9} \text{ erg s}^{-1} \text{ cm}^{-2} \text{ \AA}^{-1} \text{ sr}^{-1}$ . Although the exact value of the background light in the optical is still quite uncertain, this agreement with the best measurements thus far is encouraging. Furthermore, we know that studies of gamma-ray bursts show that the intrinsic star formation rate is a factor of three to five times higher than that measured from deep imaging surveys (Ishida et al. 2011), demonstrating that there are many faint galaxies yet to be detected at high redshifts. Figure 8, however, shows that while the faint galaxies we have not detected dominate the total number in the universe, they however do not

contribute substantially to the unresolved background optical light beyond  $m \sim 32$ .

We can, however, use this to address the issue of why the sky is dark at night, a long-standing problem known as Olbers' paradox since Bondi (1952). Our results reveal perhaps a new solution to this paradox. There are various proposed solutions to Olbers' paradox but most solutions can be placed into one of two categories: (1) there are missing stars (and/or galaxies), or (2) the stars are there, but they cannot be observed for one reason or another. Possible reasons for not detecting distant star light have included scenarios such as absorption of light, hierarchical clustering, and the removal of energy from light in an expanding universe. The traditional solution to the paradox is generally considered to be the fact that the universe is finite in age and size (Harrison 1987).

The human eye through L cone cells are sensitive out to a wavelength of 700 nm. If we consider which galaxies we would be able to see out to this wavelength, we find that galaxies out to  $z \sim 5$  would still be detected in principle. Galaxies at higher redshifts would not be detected as their light is all shifted into wavelengths longer than 700 nm or at the highest redshifts would have their light blue-ward of Ly $\alpha$  absorbed by the Ly $\alpha$  forest. At observed wavelengths bluer than this, all the light which is in principle detectable would originate within the UV continuum. However, all of this light is absorbed by gas, and perhaps dust, within the host galaxies and in the intergalactic medium near the galaxy itself, and along the site line to Earth.

Thus, it would appear from this that absorption, long discarded as one objection to Olbers' paradox, is one method for removing objects from optical light detections. This rest-frame UV light would, however, ionize hydrogen, which would then recombine, and in the process emit new light in the form of the Ly $\alpha$  line at 121.5 nm, and other lines that are mostly redder than Ly $\alpha$  (e.g., Bertone & Schaye 2012). However, this emission would be found mostly at observed near-infrared wavelengths for systems at  $z > 5$ , outside the window of visible light detections. The method of absorption thereby removes UV continuum light at wavelengths lower than the Lyman limit, and does not permit its re-introduction into the same, or bluer, wavelength range whereby it would be detectable within observed optical light. Furthermore, some of this light may also be absorbed by dust, which in the limited time range available, when the universe was only a few gigayears old at most, would then be re-emitted into the far-infrared, again outside the range of optical light.

It would thus appear that the solution to the strict interpretation of Olbers' paradox, as an optical light detection problem, is a combination of nearly all possible solutions—redshifting effects, the finite age and size of the universe, and through absorption.

#### 4.5. Implications for Future Deep Surveys

In this section we investigate future surveys and how the results of this study have implications for future studies. In the next 10 yr, we will have telescopes that will image deeper than we currently can, with the ELTs and the *James Webb Space Telescope* (JWST), and other telescopes and surveys that will cover vastly larger areas such as Euclid and LSST.

First, we answer the question of when we would expect to find the observed galaxy number counts to naturally turn over due to “running out” of faint galaxies to detect. While we are far from reaching that limit today, if we assume that the slope

of the number counts, as described in the Appendix, remains constant at magnitudes fainter than 29, we can determine at what magnitude limit we will reach the total number of actual galaxies. We do this by integrating the observed number of galaxies in the UDF using Equations (14) and (15) as a function of magnitude down to limits ranging from  $m = 20$  to  $m = 40$ . This integration allows us to infer the relationship between the total number of galaxies and the limiting magnitude reached. This relationship, shown in Figure 8, is given by

$$\log N_{\text{tot}} = (4.97 \pm 0.03) + (0.21 \pm 0.01) \times m_{\text{max}}. \quad (11)$$

We find that the magnitude limit for the total number of galaxies calculated with the mass functions (Equation (11)) is  $m_{\text{max}} \sim 34.9^{+0.6}_{-0.8}$  AB mag, taking into account the errors in the total number of galaxies. If we consider galaxies down to  $10^5$  this limit becomes  $38.9^{+0.5}_{-0.7}$ .

Based on this calculation we predict that at around magnitude 35 we would find that the observed number counts of galaxies begins to gradually decline at fainter magnitudes, unless there are a significant number of galaxies with masses  $M_* < 10^6 M_\odot$ . This depth, however, will be very difficult to reach with even very deep surveys with JWST, and may require the next generation of large space telescopes to fully probe. This would also make deep observations of future telescope observations confusion limited if they can reach these faint magnitudes.

If we want to observe all the galaxies in the universe, even with imaging, it will require extensive telescope programs that are likely several generations away. The Euclid mission planned for launch in 2020 will image 15,000 deg<sup>2</sup> down to AB magnitude of 24.5 in the wide VIS filter, which mimics in some ways the wide filter we construct in this paper using the UDF-Max image (see Appendix). The deep component of Euclid will be two magnitudes fainter over 40 deg<sup>2</sup>. Using our number counts we predict that Euclid will image around  $3.7 \times 10^9$  galaxies in total, or  $<0.1\%$  of all galaxies in the universe. This is significantly more than we have imaged at present with the Sloan Digital Sky Survey, which has imaged roughly  $1.4 \times 10^9$  galaxies and QSOs, or  $\sim 10^{-4}$  (0.05%) of all galaxies in the universe. LSST will find a similar number of galaxies. Thus we will have to wait at least several decades before even the majority of galaxies have basic imaging in a single band.

## 5. SUMMARY

We have investigated the fundamental question of the number density evolution of galaxies in the universe. We research this problem in a number of ways, and discuss the implications for galaxy evolution and cosmology. We use recently measured mass functions for galaxies up to  $z \sim 8$  to determine the number density evolution of galaxies in the universe. Our major finding is that the number densities of galaxies decrease with time such that the number density  $\phi_T(z) \sim t^{-1}$ , where  $t$  is the age of the universe.

We further discuss the implications for this increase in the galaxy number density with look-back time for a host of astrophysical questions. Integrating the number densities  $\phi_T$ , we calculate that there are  $(2.0^{+0.7}_{-0.6}) \times 10^{12}$  galaxies in the universe up to  $z = 8$ , which in principle could be observed. This is roughly a factor of 10 more than is found through direct counting (see Appendix). This implies that we have yet to detect a large population of faint distant galaxies.



In terms of astrophysical evolution of galaxies, we show that the increase in the integrated mass functions of all galaxies with redshift can be explained by a merger model. We show that a simple merger model is able to reproduce the decline in the number of galaxies with a merger timescale of  $\tau = 1.29 \pm 0.35$  Gyr. The derived merger rate at  $z = 1.5$  is  $R \sim 0.05$  mergers  $\text{Gyr}^{-1} \text{Mpc}^{-3}$ , close to the value found through structural and pair analyses. Most of these merging galaxies are lower mass systems based on the increase in number densities with time seen at lower limit selections, using higher masses, for the total number density calculation.

We finally discuss the implications of our results for future surveys. We calculate that the number counts of galaxies at magnitudes fainter than  $m_{\text{max}} = 29$  will largely probe the lower mass galaxies at higher redshifts and eventually at  $m_{\text{max}} \sim 35$  will turn over and decline due to reaching the limit of the number of galaxies in the universe, unless the mass limit for galaxies is much less than  $M_* = 10^6 M_\odot$  or there are many galaxies at  $z > 12$ . We also show that this leads to a natural confusion limit in detection and that these galaxies are likely responsible for the optical and near-infrared background and provide a natural explanation for Olbers' paradox. This large additional number of galaxies is also consistent with recent measures of the cosmic infrared background light (e.g., Mitchell-Wynne et al. 2015).

In the future, as mass functions become better known with better SED modeling and deeper and wider data with *JWST* and Euclid/LSST, we will be able to measure the total number densities of galaxies more precisely and thus obtain a better measure of this fundamental quantity.

We thank Neil Brandt, Harry Teplitz, and Caitlin Casey for useful discussions concerning non-optical deep detections in galaxy surveys. This work was supported by grants from the Royal Astronomical Society, STFC, and the Leverhulme Trust. Support was also provided by NASA/STScI grant *HST*-GO11082. A.M. acknowledges funding from a European Research Council Consolidator Grant.

## APPENDIX DIRECT GALAXY COUNTING IN THE HUBBLE ULTRA DEEP FIELD (HUDF)

In the appendix we discuss how many galaxies can be observed in the universe directly with present-day instrumentation and telescopes using the HUDF. By doing this we address how many galaxies can be detected with our present technology using the deepest observations taken to date at all wavelengths from the X-ray to the radio. We do this to compare with the model results in the main paper on the number density evolution of galaxies through cosmic time. Effectively our major results in the appendix are the number of galaxies per unit magnitude we can observe, and quantifying how many galaxies we could detect if we observed the entire sky at the same depth as the HUDF, ignoring the effects of galactic extinction. Although popular press releases have discussed this number in the past, there has never been a detailed published version of this calculation.

The HUDF image was taken with the the Advanced Camera for Surveys (ACS) on *HST* (Beckwith et al. 2006) (Section 3.1). The HUDF images are taken in the bands: F435W ( $B_{435}$ ), F606W ( $V_{606}$ ), F775W ( $i_{775}$ ), and F850L ( $z_{815}$ ). The central wavelengths of the filters we use, and their FWHM are F435W

(4297, 1038 Å), F606W (5907, 2342 Å), F775W (7764, 1528 Å), and F850L (9445, 1229 Å).

The original HUDF imaging program used 400 orbits of Hubble time for a total exposure time of just under 1 Ms. Later additions of data were added over the years by programs such as Bouwens et al. (2012). The field of view of the ACS image for the HUDF is 11 arcmin<sup>2</sup>. Detailed examination of the HUDF imaging from previous work shows that the original magnitude limit for point sources is  $m_{\text{AB}} \sim 28.5$  in the  $z$ -band at  $8\sigma$  depth using a  $0''.5$  aperture (e.g., Beckwith et al. 2006), with increased data driving this depth even fainter. This makes the HUDF easily the deepest optical imaging taken to date.

The result for the number of galaxies that can be observed with current technology, which we calculate, is largely based on these HUDF observations and through using simulations to carry out corrections for incompleteness. Estimates of this number from simply counting in deep fields has been provided in the past (e.g., Beckwith et al. 2006; Coe et al. 2006), yet we carry out this analysis in a different and more complete and careful way.

To do this calculation, we create a maximal depth HUDF image from which we carry out our counting analysis. We are also very careful to not only detect the faintest galaxies, but also to ensure that single galaxies are not overseparated into separate systems or “shredded” by the source extraction.

We supplement these counts with lower redshift counting where the HUDF area is not large enough to obtain a representative volume, as well as considerations for galaxies that are not detectable in observed optical wavelengths. First, we discuss in this section the number of galaxies retrieved through direct detections in a combined maximum depth optical HUDF image, where the bulk of galaxies in this field, which can be detected, are found.

### A.1. The Maximum Ultra-Deep Field Image (UDF-Max)

To maximize the signal-to-noise of the HUDF imaging we combine the four imaging bands—*BViz* into one band that we call the “UDF-Max” image. We add these images together according to their relative weights of signal-to-noise ratio (S/N) from their individual weight maps, and after ensuring that the point-spread function (PSF) is matched between the bands. The relative weights are determined from the depth of observations in each band, such that the combination produces the highest possible S/N in the resulting combined data. That is, these are added together according to their depth so as to maximize the signal-to-noise of the average galaxy. This will affect galaxies that are only detected in the redder/bluer bands, but we later discuss how we can ensure that these very red galaxies are still detected. The formula we use to create this maximum depth image is given by

$$\text{UDF} - \text{Max} = 1.95 \times B + 0.924 \times V + 1.98 \times i + 4.12 \times z \quad (12)$$

where UDF-Max is the new HDF-Max image, and *BViz* are the filters that are combined together. We then recalibrate this combined image to obtain a new zero point of  $M_0 = 26.4$  in AB magnitude units. This was done by converting counts per second in each band to a flux and then determining the zero point based on this flux combination. We then compute

magnitudes in our constructed UDF-Max image as follows:

$$m_{\max} = -2.5 \log C_{\max} + 26.4 \quad (13)$$

where  $C_{\max}$  is the counts per second on the UDF-Max image. These magnitudes are then measured, and later used to calculate the total number of galaxies using the number counts of galaxies at each magnitude. We furthermore checked that all the objects detected in each individual band are also detected in the combined image. This is to ensure that, for example, galaxies detected only in the  $z$ -band as, e.g., high-redshift drop out galaxies are also detected in the UDF-Max image. This was indeed the case for all galaxies down to the detection limit in each band.

After creating this optimal maximal deep image, we then detect the galaxies within it. Our method of finding galaxies in the UDF-Max, as well as for determining our completeness corrections, is done using the SExtractor detection package (Bertin & Arnouts 1996) using AUTO-MAG magnitudes. A simple detection runthrough on the  $z$ -band image finds that there are between 9000 and 10,000 galaxies within the HUDF (see also Beckwith et al. 2006), but this does not take into account incompleteness. To optimize the number of galaxies we detect, and are able to successfully extract and deblend from each other, we adjust the SExtractor detection and separation parameters accordingly. We do this through an iterative process whereby we change the SExtractor detection and deblending parameters such that galaxies are SExtracted independently from each other. That is, we repeat our detection methods until the faintest galaxies are detected and deblended. This is done while at the same time ensuring that noise is not being detected as false positive objects.

Ultimately we detect our objects in the UDF-Max using a threshold of  $1.7\sigma$ , and a minimum detection area of 5 pixels. The deblending parameters responsible for separating nearby objects from each other are set to 32 deblending sub-thresholds with a minimum contrast parameter of 0.05. We also combine the weight images from each of the four filter observations as above to remove noise that is otherwise detected as real objects by SExtractor. We find using our methods described above that there are 9713 galaxies detected in the UDF-Max. The distribution of the counts of the galaxies in the UDF-Max at a given magnitude is shown as black circles in Figure 9. If we slightly tweak this value due to changing the detection parameters we get a variation on the few-percent level in the number of galaxies detected.

However, this is just a raw number, and to obtain the total number of galaxies that are observable down to the depth of the UDF-Max, we must correct this measurement for the incompleteness of our observations. As such we carry out a series of simulations, matching the properties of high-redshift galaxies, to determine the fraction of systems we are missing when carrying out these measurements.

#### A.1.1. UDF-Max Completeness

Figure 10 shows the detection completeness from simulating galaxies within our UDF-Max image. We compute this by simulating galaxy images at a given angular size, magnitude, and surface brightness profile as fake images, and then randomly placing these into the UDF-Max image. We then detect these with the same SExtractor method and parameters as we use for the detection of the real galaxies. The

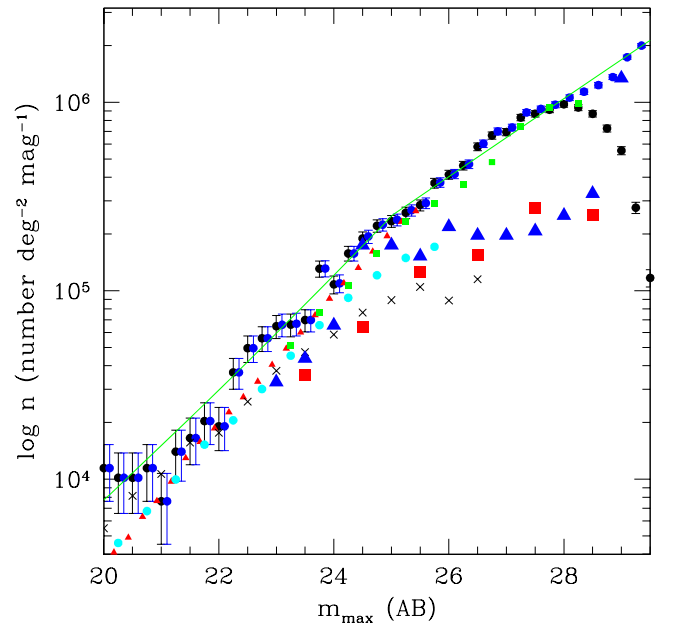


**Figure 9.** Plot showing the number counts of galaxies ( $n$ ) within the UDF-Max as a function of magnitude (see Appendix A.1.2). The black points show the raw counts of observed galaxies as a function of magnitude while the blue circle points show the corrected counts for exponential-like profiles. Also shown here for comparison are number counts measured in the red and infrared. The small red triangles are from Capak et al. (2007) using the  $i$ -band from the COSMOS survey, while the cyan circles are from Metcalfe et al. (2006). The black crosses are from the  $H$ -band GOODS NICMOS Survey (GNS; Conselice et al. 2011), the red boxes are from the Hubble Deep Field South  $H$ -band (Metcalfe et al. 2006), and the large blue triangles are from the Hubble Deep Field North (Thompson et al. 1999). Note how our points from the UDF-Max are all shifted to brighter fluxes, meaning that for the same galaxy, the magnitude is brighter in the HDF-Max than in any individual band.

completeness is then defined as the number of simulated galaxies detected divided by the total number put into the image at a given magnitude.

When carrying out these simulation, we ensure that the angular size distribution at a given magnitude of the objects we input into each simulation is the same as the observed distribution from our original SExtractor detections. To carry this out we measure the angular sizes of our galaxies through Kron radii measured through SExtractor, which we then later use in our distribution for the simulated galaxy angular sizes. We do this by fitting the observed angular size–magnitude relation and then simulating these galaxies such that they follow the same relationship, and to have the same scatter as measured statistically.

At the faintest magnitudes we assume that the size distribution is similar in shape to brighter magnitudes, but with a different average value as suggested by the relationship between magnitude and size, so as not to bias against large but fainter systems that would not be detected in our imaging. That is, we assume that the slope of the relationship between galaxy magnitude and size remains in place to our faint limit. Thus, we are allowing for sizes of systems that would not ordinarily be detected at the highest redshifts due to surface brightness dimming by assuming a similar distribution of sizes as seen at slightly lower redshifts.

We carry out these simulations using different mixtures of surface brightness profile types for the simulated galaxies. We then place these simulated galaxies in the UDF-Max image after convolving with the PSF. We then measure the

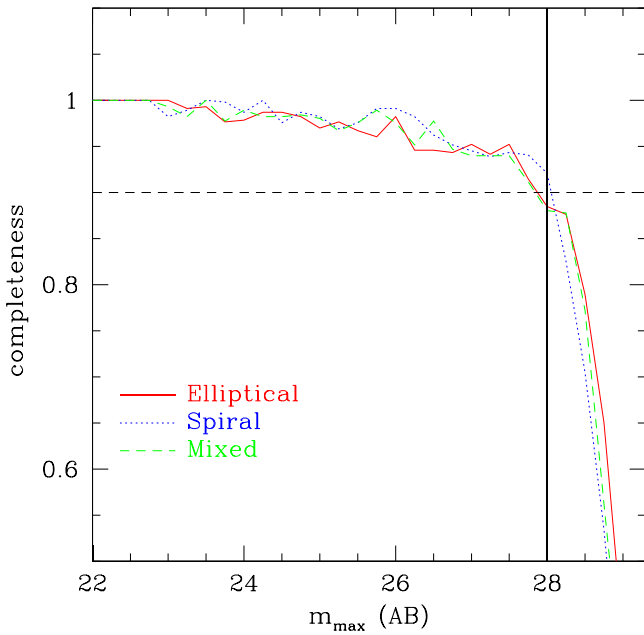


**Figure 10.** Detection fraction for galaxies within the UDF-Max based on simulations of placing fake galaxies of the same size distribution as objects within the UDF-Max and using three different light profile shapes. The red solid line shows systems that have light profiles of ellipticals, the blue dotted line shows disk profiles, and the green dashed line is an equal mixture of both.

completeness of these simulations when we use pure elliptical (i.e., Vaucouleur) profiles for all galaxies, pure exponential disk profiles, and a 50/50 split of both. Observations show that most high- $z$  galaxies have flatter profile shapes (e.g., Ferguson et al. 2004; Ravindranath et al. 2004; Buitrago et al. 2013), although we explore this range as a source of error. Each of these simulations is carried out, and the detection and incompleteness is calculated. This spans the possible range of intrinsic galaxy profiles. Based on this, the completeness of our imaging drops quickly at magnitudes fainter than  $m_{\text{max}} = 28$ , and by magnitude 30 very few galaxies are still retrieved from our detection methods. This is similar in pattern to the individual bands of the HUDF as shown by Beckwith et al. (2006).

#### A.1.2. Correct Observed Numbers

To account for the incompleteness in our detected galaxies, and thus to obtain a true total number of galaxies in the UDF-Max, we divide the completeness into the number of observed galaxies at a given magnitude. The result of the number counts before and after using this incompleteness correction is shown in Figure 9. We also show the best-fitting relationship between the number density and magnitude as a green line. This best-fitting relation has a break at  $m_{\text{max}} = 25$ . The best-fitting relation at  $m_{\text{max}} < 25$  is

$$\log n(m) = 0.048 \pm 0.001 \times \text{mag}^{1.47 \pm 0.05} \quad (14)$$

while for  $\text{mag} > 25$  the relation is

$$\log n(m) = 0.244 \pm 0.003 \times \text{mag}^{0.96 \pm 0.03}. \quad (15)$$

We then use these relations to calculate the total number density down to magnitude 29, where our detection completeness is  $>50\%$ . By integrating our magnitude fits in the UDF-

Max from  $m_{\text{max}} = 20$ –29, we calculate that the total number densities of galaxies, based on just the UDF-Max image, is  $5.7^{+0.8}_{-0.7} \times 10^6$  galaxies  $\text{deg}^{-2}$ , which is equivalent to  $\sim 1600$  galaxies  $\text{arcmin}^{-2}$  or  $\sim 0.43$  galaxies  $\text{arcsec}^{-2}$ . Using just this number density in the UDF-Max, we calculate the total number of observable galaxies in the universe at optical wavelengths as

$$N_{\text{tot,obs,opt}} = 2.34^{+0.36}_{-0.32} \times 10^{11} \text{ galaxies.}$$

This uncertainty is solely based on number counting statistics, and as such does not account for other sources of error such as nearby and very distant ( $z > 8$ ) galaxies, non-optical detections, and cosmic variance, which we discuss later in the following sections. Our number also does not differ substantially from what can be derived from the original number counts from HDF and UDF (e.g., Williams et al. 1996; Beckwith et al. 2006).

These are the results when we simulate our galaxies as systems with purely disk-like profiles. This is in fact an accurate description of distant galaxies, as disk-like profiles become increasingly common at higher redshifts, including for the most massive systems (e.g., Ferguson et al. 2004; Ravindranath et al. 2004; Buitrago et al. 2013). To obtain a measurement of our uncertainties, we recalculate this number for simulated profiles which are 100% elliptical-like profiles and for a 50/50 split between disk-like systems and elliptical-like ones. We find using these different simulation corrections that the total number of galaxies is  $2.36$  and  $2.57 \times 10^{11}$  respectively, with very similar number counting errors as found in the pure disk-like simulations. We therefore take the average of these two and use the difference as another source of error. This gives us a total number of galaxies of  $2.46^{+0.38}_{-0.34} \times 10^{11}$  galaxies.

This is, however, an underestimate of the number of galaxies potentially observable. We have also not yet taken into account the fact that the HUDF does not include the most distant objects in the universe, which are undetected in the optical, as well as the nearest galaxies, which are absent due to the nearby volume probed being very small in the UDF-Max. Although these numbers are small and make little difference to the overall total number of galaxies, we include them for completeness.

#### A.1.3. Ultra-high-redshift and Nearby Galaxies

We include the nearest galaxies in our calculation based on stellar mass functions measured for local galaxies, as well as the deepest *HST* data in the WFC3 to measure the ultra-high-redshift systems, which may exist at  $z > 8$ .

We use one of the latest deepest ultra-high-redshift searches from the UDF12 project from Ellis et al. (2013). This is a medium-band survey of the UDF done with the WFC3 near-infrared camera. By going very deep WFC3 has made it easier to find ultra-high-redshift galaxies than can be found within the ACS imaging. This deep WFC3 data has allowed Ellis et al. (2013) to identify in total seven galaxies between redshifts  $z = 8$ –12 that were previously unidentified. Assuming that this is a representative number density across the sky, the total number of galaxies that are visible to us at this redshift range is  $2.2 \pm 0.03 \times 10^8$  galaxies.

For galaxies in the nearby universe ( $z \sim 0$ ) we use the mass functions calculated in the GAMA survey by Baldry et al. (2012). The effective mid-redshift for the  $143 \text{ deg}^2$  covered in this study is  $z \sim 0.03$ , which includes 5210 galaxies. The



derived stellar mass function is best fit by a double Schechter function. Integrating this we calculate the number density within the mass limits of  $M_* = 10^6\text{--}10^{12} M_\odot$ . Doing this calculation we find that there are  $\sim 2.9 \times 10^8$  galaxies at  $z < 0.3$  that are not accounted for in the UDF-Max imaging. Likewise, we also remove the small number of galaxies in the UDF-Max imaging at  $z < 0.3$  so as not to double count the number of galaxies at these lowest redshifts.

#### A.1.4. Non-optical Wavelength Detections

While nearly all galaxies in the universe at  $z < 6$  are detectable within observed optical light, as far as we know, it is possible or even likely that there are galaxies at other wavelengths that cannot be detected in the optical and near-infrared.

First we investigate the number of galaxies that are detected at the sub-millimeter (sub-mm) and in the radio, but which are seen neither in the optical nor in the near-infrared. The latest surveys of sub-mm galaxies from Alberts et al. (2013) find that 85% of all sources have optical or near-infrared counterparts in deep GOODS imaging. Using the number densities from Casey et al. (2014), we find that between 0.1 and 1 mJy there are  $6.2 \pm 0.05 \times 10^8$  extra galaxies across the sky not matched to optical or near-infrared detections. Although the GOODS data is almost as deep as the UDF, we cannot be sure that these sources would not be found on the slightly deeper data, so we do not include them in our total number.

In terms of ultraviolet detections, a recent survey by Teplitz et al. (2013) took very deep UV imaging of the HUDF. Matching to the deep *B*-band HUDF data Teplitz et al. (2013) finds that there are no systems in the ultraviolet that do not have an optical counterpart. Extragalactic X-ray sources are similarly almost always detected in the optical/near-infrared. The currently deepest X-ray data find that 716 out of 740 (96.8%) of X-ray sources down to  $\sim 3 \times 10^{-17} \text{ erg cm}^{-2} \text{ s}^{-1}$  over 464.5 arcmin<sup>2</sup> at 0.5–8 keV are detected in deep optical data as part of the deepest 4 Ms *Chandra* imaging of the universe (Xue et al. 2011) in the HUDF area. This gives us a total of  $7.67 \pm 1.6 \times 10^6$  X-ray sources in the universe that are not accounted for by optical and/or near-infrared counterparts at the UDF-Max depth. This is much smaller than the sub-mm or optical dropout high-*z* galaxies, and thus are not likely a major contributor to the number of galaxies in the universe.

Therefore, in total we find that there are an additional  $\sim 10^9$  galaxies that must be accounted for that are not detected in the optical at  $m < 29$ . This is, however, only 1% of the nominal value we obtained for the optical detections. This implies that around 1% of galaxies that can be seen over all wavelengths are not detectable within deep *HST* imaging to the depth of HUDF.

Our final number of galaxies currently detectable within the universe with a hypothetical all-sky *HST* survey at UDF-Max depth is therefore

$$N_{\text{tot,obs,cor}} = 2.47^{+0.38}_{-0.34} \times 10^{11}.$$

These results, however, do not account for cosmic variance, which we discuss in the next section, and which is an added source of uncertainty on this measurement.

#### A.2. Cosmic Variance

One of the things we must consider in an analysis such as this is the fact that we are only probing a very small part of the

sky when examining the UDF-Max. It is certain that we would obtain a different answer if we were to repeat this experiment by investigating galaxy counts in another unrelated part of the sky/universe, obtaining a slightly higher or smaller number of counts. This is due to the fact that the distribution of galaxies can vary significantly as structure is highly clustered, and thus some regions are more overdense than others.

We can determine the contribution of this unknown random error to our results by considering both the variance due to Poisson counting errors, as well as this cosmic variance by using halo models of the universe. To do this we utilize the cosmic variance code written by Trenti & Stiavelli (2008) to determine for our observed sample the combined variance due to Poisson uncertainty and to cosmic variance.

The total variance changes significantly with the galaxy type and redshift. At the highest redshifts, this relative variance can be as much as 0.31, while at lower redshifts it is around 0.05. The variance tends to decline at lower redshifts as more representative galaxies are being studied, which lowers the amount of cosmic variance. Taking this into account in total we calculate that the cosmic variance on our measured counts is  $1.53 \times 10^{10}$  galaxies. This then gives a combined uncertainty of

$$N_{\text{tot,obs,cor} \pm \text{CV}} = 2.47^{+0.41}_{-0.37} \times 10^{11},$$

which is our final estimate of the number of galaxies we can observe today with current technology at HUDF depths in the universe (ignoring magnification by lensing and extinction) with uncertainties included for non-optical detections and cosmic variance.

## REFERENCES

- Alam, S., Albareti, F. D., Allende Prieto, C., et al. 2015, *ApJS*, **219**, 12
- Alberts, S., Wilson, G. W., Lu, Y., et al. 2013, *MNRAS*, **431**, 194
- Baldry, I. K., Driver, S. P., Loveday, J., et al. 2012, *MNRAS*, **421**, 621
- Beckwith, S., Stiavelli, M., Koekemoer, A. M., et al. 2006, *AJ*, **132**, 1792
- Bernstein, R. A. 2007, *ApJ*, **666**, 663
- Bertin, E., & Arnouts, S. 1996, *A&AS*, **117**, 393
- Bertone, S., & Schaye, J. 2012, *MNRAS*, **419**, 780
- Bimboim, Y., & Dekel, A. 2003, *MNRAS*, **345**, 349
- Bluck, A., Conselice, C. J., Buitrago, F., et al. 2012, *ApJ*, **747**, 34
- Boada, S., et al. 2015, *ApJ*, **803**, 104
- Bondi, H. 1952, *Cosmology* (Cambridge: Cambridge Univ. Press)
- Bouwens, R., Illingworth, G., Blakeslee, J. P., Broadhurst, T., & Franx, M. 2004, *ApJL*, **611**, L1
- Bouwens, R. J., Illingworth, G. D., Franx, M., & Ford, H. 2008, *ApJ*, **686**, 230
- Bouwens, R. J., Illingworth, G. D., Franx, M., et al. 2009, *ApJ*, **705**, 936
- Bouwens, R. J., Illingworth, G. D., Oesch, P. A., et al. 2011, *ApJ*, **737**, 90
- Bouwens, R. J., Illingworth, G. D., Oesch, P. A., et al. 2012, *ApJ*, **754**, 83
- Bouwens, R. J., Illingworth, G. D., Oesch, P. A., et al. 2015, *ApJ*, **803**, 34
- Bridge, C. R., Appleton, P. N., Conselice, C. J., et al. 2007, *ApJ*, **659**, 931
- Buitrago, F., Trujillo, I., Conselice, C. J., & Haussler, B. 2013, *MNRAS*, **428**, 1460
- Capak, P., Aussel, H., Ajiki, M., et al. 2007, *ApJS*, **172**, 99
- Caputi, K. I., Cirasuolo, M., Dunlop, J. S., et al. 2011, *MNRAS*, **413**, 162
- Casey, C. M., Narayanan, D., & Cooray, A. 2014, *PhR*, **541**, 45
- Coe, D., Benitez, N., Sanchez, S., et al. 2006, *AJ*, **132**, 926
- Conselice, C. J. 2006, *ApJ*, **638**, 686
- Conselice, C. J. 2014, *ARA&A*, **52**, 291
- Conselice, C. J., & Arnold, J. 2009, *MNRAS*, **397**, 208
- Conselice, C. J., Bluck, A. F. L., Buitrago, F., et al. 2011, *MNRAS*, **413**, 80
- Conselice, C. J., Grogin, N. A., Jogee, S., et al. 2004, *ApJ*, **600**, 139
- Conselice, C. J., Rajgor, S., & Myers, R. 2008, *MNRAS*, **386**, 909
- Djorgovski, S., Soifer, B. T., Pahre, M. A., et al. 1995, *ApJ*, **438**, 13
- Dominguez, A., Primack, J. R., Rosario, D. J., et al. 2011, *MNRAS*, **410**, 2556
- Duffy, A., Wyithe, J. S. B., Mutch, S. J., & Poole, G. B. 2014, *MNRAS*, **443**, 3435
- Duncan, K., & Conselice, C. J. 2015, *MNRAS*, **451**, 2030
- Duncan, K., Conselice, C. J., Mortlock, A., et al. 2014, *MNRAS*, **444**, 2960



- Ellis, R. S., McLure, R. J., Dunlop, J. S., et al. 2013, *ApJ*, **763**, 7
- Ferguson, H. C., Dickinson, M., Giavalisco, M., et al. 2004, *ApJ*, **600**, 107
- Finkelstein, S. L., Ryan, R. E., Jr., Papovich, C., et al. 2015, *ApJ*, **810**, 71
- Fontana, A., Pozzetti, L., Donnarumma, I., et al. 2004, *A&A*, **424**, 23
- Fontana, A., Salimbeni, S., Grazian, A., et al. 2006, *A&A*, **459**, 745
- Foreman-Mackey, D., Hogg, D. W., Lang, D., & Goodman, J. 2013, *PASP*, **125**, 925
- Fressin, F., Torres, G., Charbonneau, D., et al. 2013, *ApJ*, **766**, 81
- Fukugita, M., & Peebles, P. J. E. 2004, *ApJ*, **616**, 643
- Genel, S., Vogelsberger, M., Springel, V., et al. 2014, *MNRAS*, **445**, 175
- Giavalisco, M., Ferguson, H. C., Koekemoer, A. M., et al. 2004, *ApJ*, **600**, 93
- Gonzalez-Perez, V., Lacey, C. G., Baugh, C. M., et al. 2014, *MNRAS*, **439**, 264
- Graus, A. S., Bullock, J. S., Boylan-Kolchin, M., & Weisz, D. R. 2015, *MNRAS*, **456**, 477
- Grazian, A., Fontana, A., Santini, P., et al. 2015, *A&A*, **575**, 96
- Grebel, E., Gallagher, J. S., III, & Harbeck, D. 2003, *AJ*, **125**, 1926
- Grogin, N., et al. 2011, *ApJS*, **197**, 35
- Harrison, E. 1987, *Darkness at Night: A Riddle of the Universe* (Cambridge, MA: Harvard Univ. Press)
- Henriques, B. M. B., White, S. D. M., Thomas, P. A., et al. 2015, *MNRAS*, **451**, 2663
- Ibata, R. A., et al. 2013, *Natur*, **493**, 62
- Ishida, E. E. O., de Souza, R. S., & Ferrar, A. 2011, *MNRAS*, **418**, 500
- Jenkins, A., Frenk, C. S., White, S. D. M., et al. 2001, *MNRAS*, **321**, 372
- Jogee, S., Miller, S. H., Penner, K., et al. 2009, *ApJ*, **697**, 1971
- Kajisawa, M., Ichikawa, T., Tanaka, I., et al. 2009, *ApJ*, **702**, 1393
- Koekemoer, A., Faber, S. M., Ferguson, H. C., et al. 2011, *ApJS*, **197**, 36
- Koo, D., & Kron, R. 1992, *ARA&A*, **30**, 613
- Laporte, N., Streblyaska, S. K., Pelló, R., et al. 2015, *A&A*, **575**, A92
- Lee, B., Giavalisco, M., Williams, C. C., et al. 2013, *ApJ*, **774**, 47
- Lin, L., Koo, D. C., Weiner, B. J., et al. 2007, *ApJ*, **660**, 51
- Lin, L., Patton, D. R., Koo, D. C., et al. 2008, *ApJ*, **681**, 232
- Livermore, R. C., Finkelstein, S. L., & Lotz, J. 2016, arXiv:1604.06799
- Lotz, J. M., Jonsson, P., Cox, T. J., et al. 2011, *ApJ*, **742**, 103
- Luo, B., Brandt, W. N., Xue, Y. Q., et al. 2010, *ApJS*, **187**, 560
- Madau, P., & Dickinson, M. 2014, *ARA&A*, **52**, 415
- Marchesini, D., van Dokkum, P. G., Förster Schreiber, N. M., et al. 2009, *ApJ*, **701**, 1765
- McLure, R., Cirasuolo, M., Dunlop, J. S., Foucaud, S., & Almaini, O. 2009, *MNRAS*, **395**, 2196
- McLure, R., Dunlop, J. S., Bowler, R. A. A., et al. 2013, *MNRAS*, **432**, 2696
- Metcalf, N., Shanks, T., Campos, A., McCracken, H. J., & Fong, R. 2001, *MNRAS*, **323**, 795
- Metcalf, N., Shanks, T., Weilbacher, P. M., et al. 2006, *MNRAS*, **370**, 1257
- Mitchell-Wynne, K., Asantha, C., Gong, Y., et al. 2015, *NatCo*, **6**, 7945
- Mortlock, A., Conselice, C. J., Bluck, A. F. L., et al. 2011, *MNRAS*, **413**, 2845
- Mortlock, A., Conselice, C. J., Hartley, W. G., et al. 2013, *MNRAS*, **433**, 1185
- Mortlock, A., Conselice, C. J., Hartley, W. G., et al. 2015, *MNRAS*, **447**, 2
- Muzzin, A., Marchesini, D., Stefanon, M., et al. 2013, *ApJ*, **777**, 18
- Ono, Y., et al. 2013, *ApJ*, **777**, 155
- Owensworth, J. R., Conselice, C. J., Mortlock, A., et al. 2014, *MNRAS*, **445**, 2198
- Papovich, C., Dickinson, M., Giavalisco, M., Conselice, C. J., & Ferguson, H. C. 2005, *ApJ*, **631**, 101
- Penny, S. J., & Conselice, C. J. 2008, *MNRAS*, **383**, 247
- Perez-Gonzalez, P., Trujillo, I., Barro, G., et al. 2008, *ApJ*, **687**, 50
- Pozzetti, L., Bolzonella, M., Lamareille, F., et al. 2007, *A&A*, **474**, 443
- Ravindranath, S., Ferguson, H. C., Conselice, C. J., et al. 2004, *ApJ*, **604**, 9
- Robertson, B. E., Ellis, R. S., Furlanetto, S. R., & Dunlop, J. S. 2015, *ApJ*, **802**, 19
- Schechter, P. 1976, *ApJ*, **203**, 297
- Song, M., Finkelstein, S. L., Ashey, M. L. N., et al. 2016, *ApJ*, **825**, 5
- Steidel, C., & Hamilton, D. 1992, *AJ*, **104**, 941
- Teplitz, H., Rafelski, M., Kurczynski, P., et al. 2013, *AJ*, **146**, 159
- Thompson, R., Beckwith, S. V. W., Fockenbrock, R., et al. 1999, *ApJ*, **523**, 100
- Tomczak, A. R., Quadri, R. E., Tran, K.-V. H., et al. 2014, *ApJ*, **783**, 85
- Torrey, P., Wellons, S., Machado, F., et al. 2015, *MNRAS*, **454**, 2770
- Trenti, M., & Stiavelli, M. 2008, *ApJ*, **676**, 767
- Vogelsberger, M., Genel, S., Springel, V., et al. 2014, *Natur*, **509**, 177
- Weigel, A. K., Schawinski, K., & Bruderer, C. 2016, *MNRAS*, **459**, 2150
- Williams, R., Baum, S., Bergeron, L. E., et al. 2000, *AJ*, **120**, 2735
- Williams, R., Blacker, B., Dickinson, M., et al. 1996, *AJ*, **112**, 1335
- Xue, Y. Q., Luo, B., Brandt, W. N., et al. 2011, *ApJS*, **195**, 10